AGU PUBLICATIONS

JGR

Journal of Geophysical Research: Solid Earth

RESEARCH ARTICLE
10.1002/2014JB011478

Key Points:
- Cordón Caulle event exhibits transitional features from strong to weak plumes
- Cloud spreading was described by gravitational intrusion and turbulent diffusion
- Density-driven transport is important even for small wind-advected clouds

Supporting Information:
- Figures S1–S4 and Tables S1–S7

Correspondence to:
C. Bonadonna,
costanza.bonadonna@unige.ch

Citation:
Bonadonna, C., M. Pistolesi, R. Cioni, W. Degruyter, M. Elissondo, and V. Baumann (2015), Dynamics of wind-affected volcanic plumes: The example of the 2011 Cordón Caulle eruption, Chile, *J. Geophys. Res. Solid Earth*, *120*, 2242–2261, doi:10.1002/2014JB011478.

Received 23 JUL 2014
Accepted 2 MAR 2015
Accepted article online 6 MAR 2015
Published online 17 APR 2015

Dynamics of wind-affected volcanic plumes: The example of the 2011 Cordón Caulle eruption, Chile

C. Bonadonna[1], M. Pistolesi[2], R. Cioni[2], W. Degruyter[3], M. Elissondo[4], and V. Baumann[4]

[1]Section des Sciences de la Terre et de l'Environnement, Universitè de Genève, Geneva, Switzerland, [2]Dipartimento di Scienze della Terra, Università di Firenze, Firenze, Italy, [3]Earth and Atmospheric Sciences, Georgia Tech, Atlanta, Georgia, USA, [4]Servicio Geológico Minero Argentino, Buenos Aires, Argentina

Abstract The 2011 Cordón Caulle eruption represents an ideal case study for the characterization of long-lasting plumes that are strongly affected by wind. The climactic phase lasted for about 1 day and was classified as subplinian with plumes between ~9 and 12 km above the vent and mass flow rate (MFR) on the order of ~10^7 kg s^{-1}. Eruption intensity fluctuated during the first 11 days with MFR values between 10^6 and 10^7 kg s^{-1}. This activity was followed by several months of low-intensity plumes with MFR $< 10^6$ kg s^{-1}. Plume dynamics and rise were strongly affected by wind during the whole eruption with negligible upwind spreading and sedimentation. The plumes that developed on 4–6 and 20–22 June can be described as transitional, i.e., plumes showing transitional behavior between strong and weak dynamics, while the wind clearly dominated the rise height on all the other days resulting in the formation of weak plumes. Individual phases of the eruption range between Volcanic Explosivity Indices (VEIs) 3 and 4, while the cumulative deposit related to 4–7 June 2011 is associated with VEIs 4 and 5. Crosswind cloud and deposit dispersal of the first few days are best described by a linear combination of gravitational spreading and turbulent diffusion, with velocities between 1 and 10 m s^{-1}. Downwind cloud velocity for the same days is best described by a linear combination of gravitational spreading and wind advection, with velocities between 17 and 45 m s^{-1}. Results show how gravitational spreading can be significant even for subplinian and small-moderate eruptions strongly advected by wind and with low Richardson number and low MFR.

1. Introduction

Fundamental volcanic processes, such as conduit and plume dynamics, abrupt transitions in eruptive regimes, and eruption unsteadiness, are currently only partially understood. This generates confusion in the way we characterize and classify eruptions, especially in the cases of small-moderate eruptions, and hinders our capability to identify potential eruptive scenarios and assess the associated hazards. The characterization and classification of volcanic eruptions are crucial to (i) our scientific understanding (i.e., to simplify a complex system by identifying leading-order processes and to aid comparison between different eruptions or volcanoes), (ii) hazard and risk assessment, and (iii) science and hazard communication [*Bonadonna et al.*, 2014]. Nonetheless, most existing classification schemes only include parameters that do not represent the full complexity of volcanic eruptions and can be associated with large uncertainties (e.g., average or maximum plume height, cumulative erupted volume, mass flow rate, and grain-size distribution) and therefore do not contribute significantly to our comprehension of the volcanic system. This is particularly true for prehistoric eruptions that occurred when no observations of the plume and of the meteorological conditions could be made. Due to the complex dynamics that characterize many eruptive events, the derivation and interpretation of these parameters are not always straightforward even for recent, directly observed eruptions, and many strategies can be applied that are associated with various degrees of uncertainty. Tephra deposits associated with long-lasting eruptions can be further complicated by the combination of varying eruptive and atmospheric conditions in time.

Here we discuss the case of the 2011 rhyolitic eruption of Cordón Caulle volcano (Chile) that caused widespread disruption to various economic sectors and human activities, representing a complex eruptive event that needs to be described in detail in order to characterize the range of the associated time-dependent eruption source parameters and mitigate future risks. Only a few rhyolitic eruptions have been studied in detail (e.g., Chaitén 2008 eruption, Chile [*Alfano et al.*, 2011; *Castro and Dingwell*, 2009; *Folch et al.*, 2008]). They are characterized by an initial climactic phase associated with both convective plumes and pyroclastic

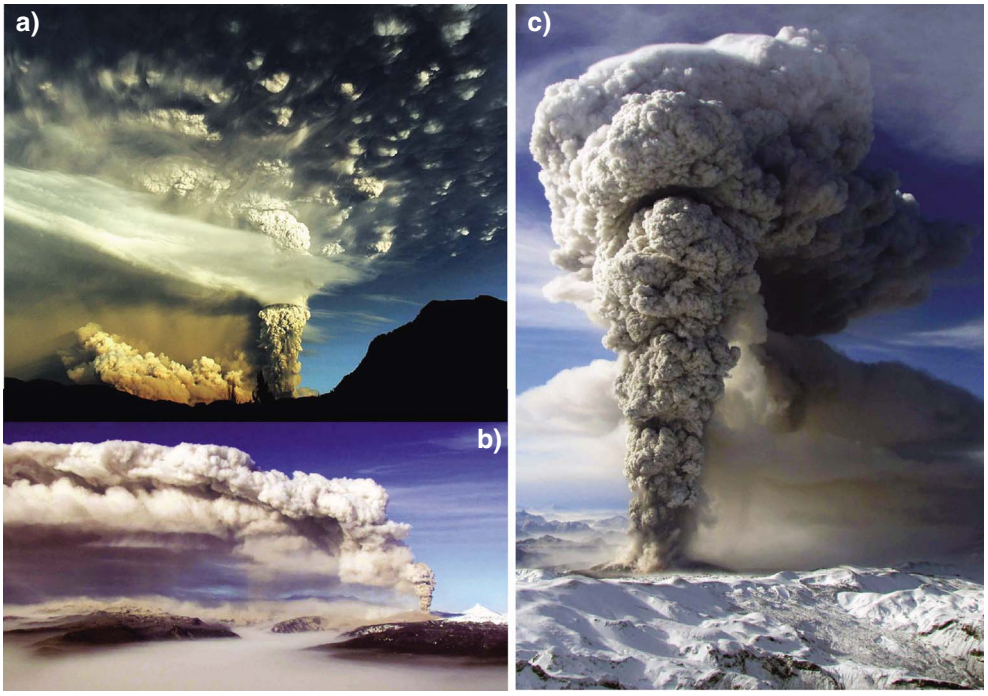

Figure 1. Volcanic plumes associated with the 2011 eruption of Cordón Caulle: (a) 4 June, plume height of ~9–12 km above the vent (also showing pyroclastic density currents) and (b and c) 13 June, plume height of ~7–9 km above the vent (Figure 1a: http://www.emol.com/noticias/internacional/2011/06/15/487543/miles-de-pasajeros-atrapados-en-nueva-zelanda-y-australia-por-ceniza-del-volcan-puyehue.html, Figure 1b: http://imagenesfotos.com/fotos-del-volcan-puyehue/, and Figure 1c: http://www.flickr.com/photos/pentadragon/).

density currents (PDCs) followed by lava effusion and monthlong low-intensity, ash-laden plumes [*Castro et al*., 2013]. The 2011 eruption of Cordón Caulle volcano also provides the unique opportunity to explore (i) the interaction between plume dynamics and atmospheric wind and (ii) the complex interplay among cloud gravitational spreading, atmospheric diffusion, and wind advection of small-moderate eruptions, which have recently been topics of lively debates within the international community [e.g., *Degruyter and Bonadonna*, 2012, 2013; *Devenish*, 2013; *Woodhouse et al*., 2013; *Costa et al*., 2013; *Carazzo et al*., 2014; *Mastin et al*., 2014]. A detailed characterization of the stratigraphy and deposit features is presented by *Pistolesi et al*. [2015], while specific aspects of tephra sedimentation and grain size are presented by *Bonadonna et al*. [2015]. Here we focus on the determination of key physical parameters of the main eruptive phases in relation to eruption classification (i.e., erupted mass, plume height, mass flow rate, and eruption duration) and on the characterization of plume dynamics and cloud spreading.

2. Eruption Chronology

Cordón Caulle, part of the Puyehue-Cordón Caulle volcanic complex located in the central Andes, produced large rhyodacitic fissure eruptions of volcanic explosivity index (VEI) 3 in 1921–1922 and 1960, whereas two VEI 5 eruptions had occurred about 860 B.P. and 5000 B.C. but were associated with the Puyehue stratovolcano (GVP, Global Volcanism Program; http://www.volcano.si.edu [*Siebert et al*., 2010]). After about 41 years of repose, an eruption started at Cordón Caulle volcano on 4 June 2011, around 18:30 UTC according to Geostationary Operational Environmental Satellite (GOES) images. The climactic phase (~27 h [*Jay et al*., 2014]) was associated with a ~9–12 km high plume (above vent, with a vent height of about 1.5 km) that dispersed most of the tephra toward E and SE (Figure 1) [*Castro et al*., 2013; *Collini et al*., 2013; *Pistolesi et al*., 2015].

The tephra deposit associated with the first week of the eruption (4–11 June 2011) was studied based on about 70 outcrops located between 1 and 240 km from the active vent and was subdivided into three

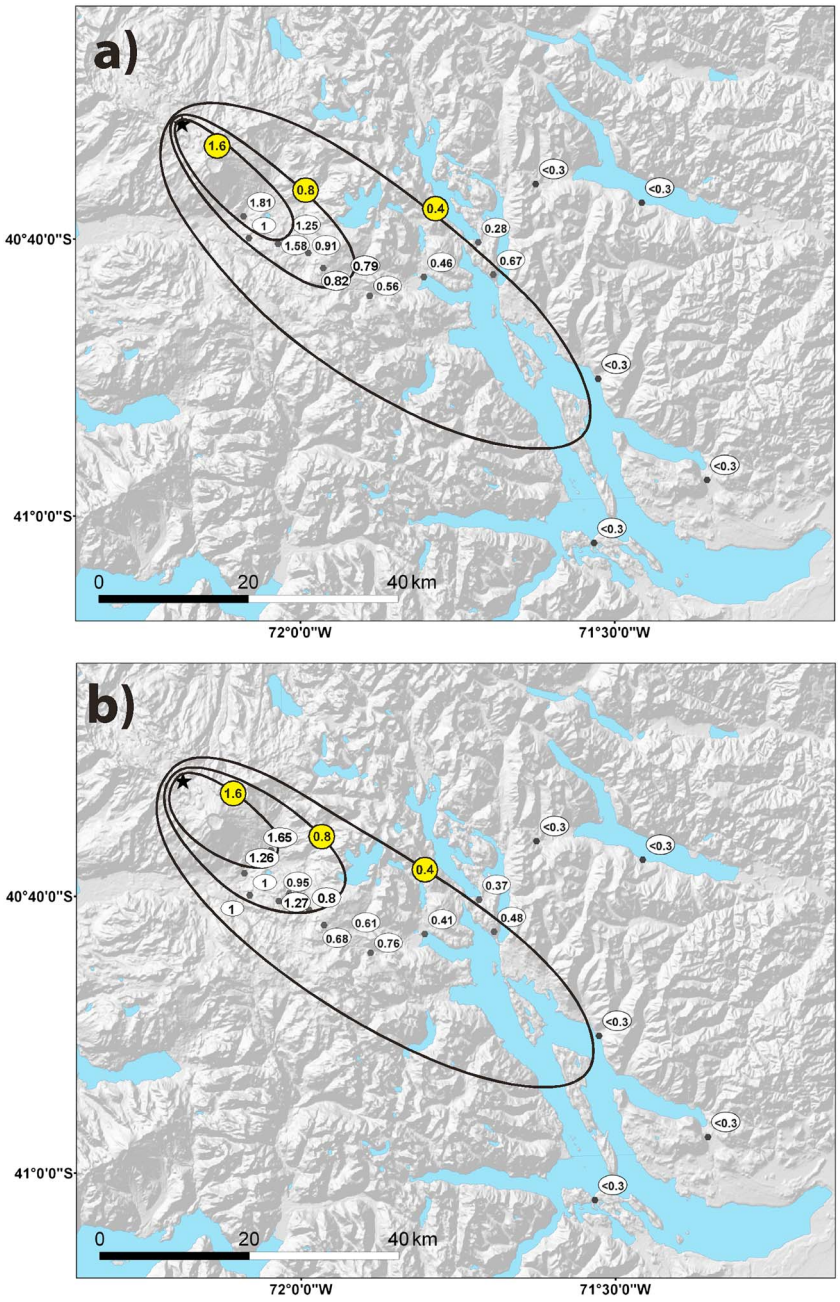

Figure 2. Isopleth map (in centimeter) of the largest lithics (LLs) for Unit I (layers A–F) based on (a) the geometric mean of the five largest clasts and (b) the 50th percentile of a 20 clast population.

main units: Unit I, layers A to F; Unit II, layers G to H; and Unit III, layers K1 to K5 (see *Pistolesi et al*. [2015] for more details on the field surveys and *Bonadonna et al*. [2015] and the supporting information for isomass maps of individual phases). In particular, Unit I was mostly deposited toward SE (4 and 5 June 2011), Unit II toward the N (5 and 6 2011), and Unit III toward the E (7–11 June 2011). Upwind sedimentation was negligible during all phases. PDCs were generated in 4, 5, 8, and 14 June (with a runout of ~10 km [*Servicio Nacional de Geología y Minería/Observatorio Volcanológico de Los Andes del Sur*, 2011]), whereas on 10 June, destructive lahars were triggered by heavy rains. Onset of lava effusion was reported on 15 June. Lava was still moving at a low rate by April 2012 [*Tuffen et al*., 2013].

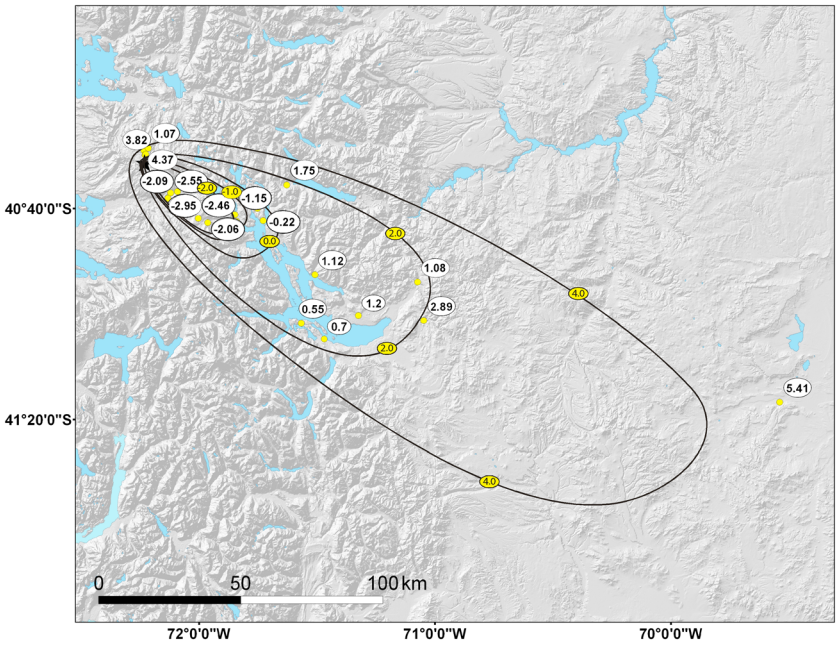

Figure 3. Mdϕ map for Unit I (cumulative layers A–F) (units in ϕ).

3. Physical Parameters and Eruption Classification

3.1. Plume Height and Wind Speed

A population of 20 lithic clasts was collected at selected outcrops; three orthogonal axes of each clast (with the approximation of the minimum ellipsoid) were measured, and the associated geometric mean (i.e., the cube root of the product of the three axes) of the 50th percentile and of the five largest clasts was determined in order to compile two isopleth maps and validate the representativeness of largest clast values [*Bonadonna et al*., 2013] (Figure 2). Selected samples were also collected for grain-size distribution. The map of median diameter Mdϕ [*Inman*, 1952] of the cumulative Unit I (layers A–F) is shown in Figure 3, while detailed grain-size analyses are reported in *Bonadonna et al*. [2015].

The two isopleth maps in Figure 2 were used to determine the maximum plume height for Unit I (cumulative layers A–F) applying the method of *Carey and Sparks* [1986]. As described in *Bonadonna et al*. [2013], the isopleth map based on the 50th percentile is expected to be more representative of the grain size variation around the volcano, but being associated with lower grain size values than the map based on the five largest clasts, it is typically associated with lower plume heights [e.g., *Biass and Bonadonna*, 2011]. Nonetheless, the two isopleth maps shown in Figure 2 are very similar, with the 0.8 and 1.6 cm being slightly more elongated for the geometric mean of the five largest lithic clasts with respect to the 50th percentile. For both maps, we obtained a maximum plume height of about 18 ± 3 km and 15 ± 3 km above sampling height (ash), i.e., mean elevation of the isopleth contours (~930 m above sea level (asl)), for the 0.8 cm and the 1.6 cm contours, respectively (the error is based on the assumption of an intrinsic 20% error for this method [*Carey and Sparks*, 1986]). A maximum wind at the tropopause of about 40 m s^{-1} was also determined for both contours and both maps. The plume height of layers A–F was also calculated based on the Weibull fit of both largest lithics (LLs) and Mdϕ [*Bonadonna and Costa*, 2013a] (Figures 2a and 3). Both isopleth maps for the lithics resulted in a plume height of about 13 ± 3 km ash, while the Mdϕ map resulted in a plume height of about 10 ± 2 km ash (still assuming a 20% intrinsic error associated with the method [*Bonadonna and Costa*, 2013a]) (Table 1). It is important to highlight that plume heights derived based on the method of *Carey and Sparks* [1986] and of *Bonadonna and Costa* [2013a] (LL strategy) are maximum (peak) values, whereas the plume heights from *Bonadonna and Costa* [2013a] (Mdϕ strategy) are average values. This is related to the fact that the LL strategies capture the most intense stage of the associated eruptive phase, while the Mdϕ strategy describes the whole deposit and tends to average the fluctuation of eruptive conditions. In addition, the method of *Carey and Sparks* [1986] is based on plume vertical velocity for strong plumes and only accounts for the effect of wind

Table 1. Physical and Classification Parameters of Main Eruptive Phases

	Layers A–B	Layers A–F	Layer H	Layer K2
Stratigraphic unit	I	I	II	III
Date	4 June	4–5 June	5–6 June	7 June
Plume height (kilometers above vent)[a]	8.5–12.2	8.5–12.2	8.5–10.7	4.0–8.3
Plume height (kilometers above sampling height)[b]	ND[d]	16 ± 3, 13 ± 3, and 10 ± 2	ND	ND
Plume height (kilometers above the vent)[c]	11.5	12.0	ND	ND
Minimum/maximum MFR ($\times 10^6$ kg s^{-1})	2.7/28.2	2.0/28.2	1.5/17.4	0.5/10.7
Average MFR ($\times 10^6$ kg s^{-1})	8.7	7.3	4.4	2.4
Mass (kg)	$1.6 \pm 0.8 \times 10^{11}$	$4.5 \pm 1.0 \times 10^{11}$	$1.3 \pm 0.4 \times 10^{11}$	$2.8 \pm 0.7 \times 10^{10}$
Minimum/maximum duration (hours)	1.6/16.6	5.5/53.9	3.2/20.9	0.7/14.4
Average duration (hours)	5.1	17.2	8.3	3.2
Magnitude	4.2	4.6	4.1	3.4
Volcanic explosivity index	4	4	4	3

[a]Plume height: observed (*Collini et al*. [2013] and GVP; supporting information).
[b]Plume height derived based on *Carey and Sparks* [1986] and *Bonadonna and Costa* [2013a] for LL and Mdϕ, respectively.
[c]Plume height derived based on inversion of mass loading.
[d]ND: Not Derivable. Vent height is 1470 m, while average sampling height is 930 m. Minimum, maximum, and average MFR is calculated based on the uncertainty on plume height and atmospheric conditions (blue bars and black circles in Figure 6a, respectively). MFR for layers A–F and H are averaged over 4 and 5 June and 5 and 6 June, respectively (Figure 6a). Mass is average erupted mass based on both empirical and analytical methods. Minimum, maximum, and average durations are derived by dividing average erupted mass by maximum, minimum, and average MFRs.

at the spreading height, while the Cordón Caulle plume was probably characterized by lower plume ascent velocity and was clearly affected by wind advection along the whole rise height (see section 3.3). This results in an overestimation of plume height.

3.2. Erupted Mass

The volume of individual phases, derived by *Pistolesi et al*. [2015] based on three empirical strategies (i.e., exponential, power law, and Weibull fits), was converted into erupted mass based on the average measured deposit density (i.e., 560 kg m^{-3} for layers A–F and 600 kg m^{-3} for layers H and K2 [*Bonadonna et al*., 2015]). Values of $1.2 \pm 0.06 \times 10^{11}$, $4.2 \pm 0.9 \times 10^{11}$, $1.3 \pm 0.4 \times 10^{11}$, and $2.8 \pm 0.7 \times 10^{10}$ kg were obtained for layers A–B, A–F, H, and K2 layers, respectively, resulting in a total mass of $5.7 \pm 1.0 \times 10^{11}$ kg (i.e., layers A–F + H + K2) (the mean and standard deviation are calculated based on the different empirical strategies used).

Erupted mass was also calculated for layers A–B and A–F based on the inversion of the advection-diffusion model TEPHRA2 [*Bonadonna et al*., 2005b] according to the downhill simplex strategy developed by *Connor and Connor* [2006] to find the best set of eruptive parameters through the comparison between observed and computed mass accumulation per unit area. The deposits of layers H and K2 were not inverted due to the relatively large fraction of fine ash that cannot be easily reproduced by TEPHRA2 without describing particle aggregation. A systematic search of minimum values of the root-mean-square error (RMSE) was carried out to assess the presence of multiple minima (Figure 4) before performing targeted inversions. The whole range of eruptive parameters explored includes erupted mass, plume height, and grain size features (i.e., Mdϕ and sorting). RMSE is a good measure of accuracy, but it is scale dependent, and therefore, it is only good to compare goodness of fit within each analysis. Due to model sensitivity and interaction with other input parameters, the erupted mass is typically better constrained than plume height [e.g., *Bonadonna and Costa*, 2013b; *Scollo et al*., 2008]. In fact, if only the coarse fraction of layers A–F is inverted (-5 to 3 ϕ), a better constraint is obtained for plume height, which is in agreement with observations (Figure 4c); however, the associated mass is related only to the coarse fraction (i.e., ~85% of the total mass [*Bonadonna et al*., 2015]). Nonetheless, also the erupted mass for both layers A–B and A–F is not as well constrained by the model as for larger eruptions (e.g., Pululagua 2450 B.P. [*Volentik et al*., 2010] and 4 ka Rungwe Pumice [*Fontijn et al*., 2011]), with many relative RMSE minima associated with both an underestimation and an overestimation of the erupted mass as derived from empirical integrations (dashed lines in Figure 4). Targeted inversions were run based on the ranges identified by both the minimum values of RMSE shown by Figure 4 and empirical observations (see supporting information for more details). The best fit of erupted mass for the whole deposit was found for values of 2.8×10^{11} kg, 5.4×10^{11} kg, and 2.0×10^{11} kg for layers A–B, A–F, and the coarse fraction of layers A–F, respectively, which are in good agreement with the mass calculated from mapped deposit

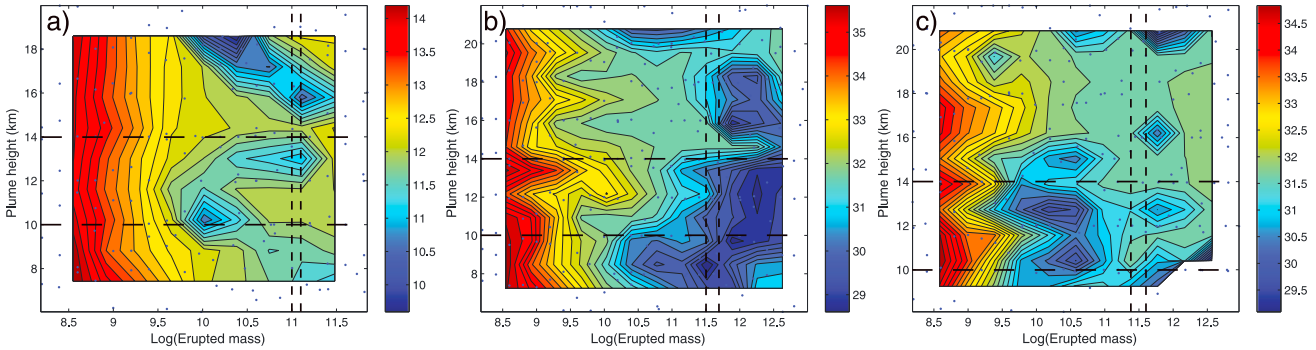

Figure 4. Plot of log(erupted mass) versus plume height (kilometer) (above sea level) showing the minimum values of the goodness-of-fit measure (root-mean-square error, RMSE; kg/m^2) for the tephra deposit associated with (a) layers A–B, (b) layers A–F, and (c) layers A–F (coarse fraction: −5 to 3ϕ). Erupted mass was varied between 10^8 and 10^{13} kg with 0.2 log(mass) increments, and the plume height was varied between 6 and 22 km with 2 km height increments. The resulting values were interpolated to produce 2-D RMSE. A scale of RMSE is also shown, with dark blue indicating the minimum values (i.e., best fit). The vertical dashed lines indicate the interval of erupted mass as obtained from empirical integrations (Table 1), while horizontal dashed lines indicate the range of observed plume heights (supporting information). Erupted mass of the coarse fraction of layers A–F is calculated as 85% of total mass from grain-size analysis of *Bonadonna et al.* [2015].

based on empirical strategies. Associated plume heights are 13.0, 13.5, and 13.1 km asl, also in agreement with observations (supporting information and Table 1). Averaging results of empirical and analytical methods, we conclude that the erupted mass associated with layers A and B and A–F are $1.6 \pm 0.8 \times 10^{11}$ and $4.5 \pm 1.0 \times 10^{11}$, respectively. The total mass for layers A–F + H + K2 becomes $6.0 \pm 1.1 \times 10^{11}$ kg.

3.3. Mass Flow Rate

A detailed account of observed plume heights during the whole eruption was compiled by both *Collini et al.* [2013] and the GVP as provided by the Buenos Aires Volcanic Ash Advisory Center and SERNAGEOMIN (03/2012 (BGVN 37:03), http://www.volcano.si.edu/volcano.cfm?vn=357150#bgvn_3703; Figure 5, Table 1, and supporting information). The interaction between plume rise and wind advection is well shown by the Aqua satellite image that captured the first development of the volcanic cloud on 4 June while it was passing over Villa La Angostura (about 40 km from the Chilean border) and by the Futangue stationary camera images between 13 and 20 June 2011 (Figure 5). All images show negligible upwind spreading, with a small inclination of the rising plume (based on the Aqua satellite image). The Aqua satellite image also highlights the heterogeneity of the volcanic cloud, with a distinct puff-like structure (~15 × 17 km) close to the vent, which is about 1.5 km higher than the main cloud (~10 km above ground; heights calculated based on cloud shadow clinometry [e.g., *Holasek and Self*, 1995]) (supporting information). Such a feature suggests a pulsating dynamics, typical of long-lasting plumes (e.g., Eyjafjallajökull 2010 plume [e.g., *Ripepe et al.*, 2013]).

MFR between 4 and 30 June 2011 was calculated between ~10^4 and ~10^7 kg s^{-1} using the method of *Degruyter and Bonadonna* [2012] that accounts for the effects of wind advection and thermal stratification of the atmosphere on the plume height (Figure 6a):

$$\mathrm{MFR} = \pi \frac{\rho_{a0}}{g'} \left(\frac{\alpha^2 \overline{N}^3}{10.9} H^4 + \frac{\beta^2 \overline{N}^2 \overline{v}}{6} H^3 \right) = \pi \frac{\rho_{a0}}{g'} \frac{\alpha^2 \overline{N}^3}{10.9} H^4 \left(1 + \frac{1}{\Pi} \right) \quad (1)$$

where H is the plume height above the vent (m), $\overline{N}$ is the average buoyancy frequency (s^{-1}) across the plume height and quantifies the thermal stratification of the atmosphere, $\overline{v}$ is the average wind velocity across the plume height (m s^{-1}), α is the radial entrainment coefficient, β is the wind entrainment coefficient, ρ_{a0} is the atmospheric density at the vent (kg m^{-3}), and g' (m s^{-2}) is equivalent to the reduced gravity based on the difference in sensible heat between the gas-pyroclast mixture and the ambient sensible heat at the source (i.e., $g' = g\left(\frac{c_0\theta_0 - c_{a0}\theta_{a0}}{c_{a0}\theta_{a0}}\right)$, where c_0, θ_0, c_{a0}, and θ_{a0} are the eruption heat capacity, eruption temperature, reference heat capacity, and reference temperature, respectively). The quantity Π is a scaling parameter and is defined below (equation (2)). For the plume height, we use the minimum and maximum values reported from all sources mentioned above (supporting information). We use the wind, humidity, temperature, and pressure data provided by ECMWF (European Centre for Medium-Range Weather Forecasts) ERA-Interim at a 0.25° resolution [*Dee et al.*, 2011] and calculate the average wind speed across the plume height using

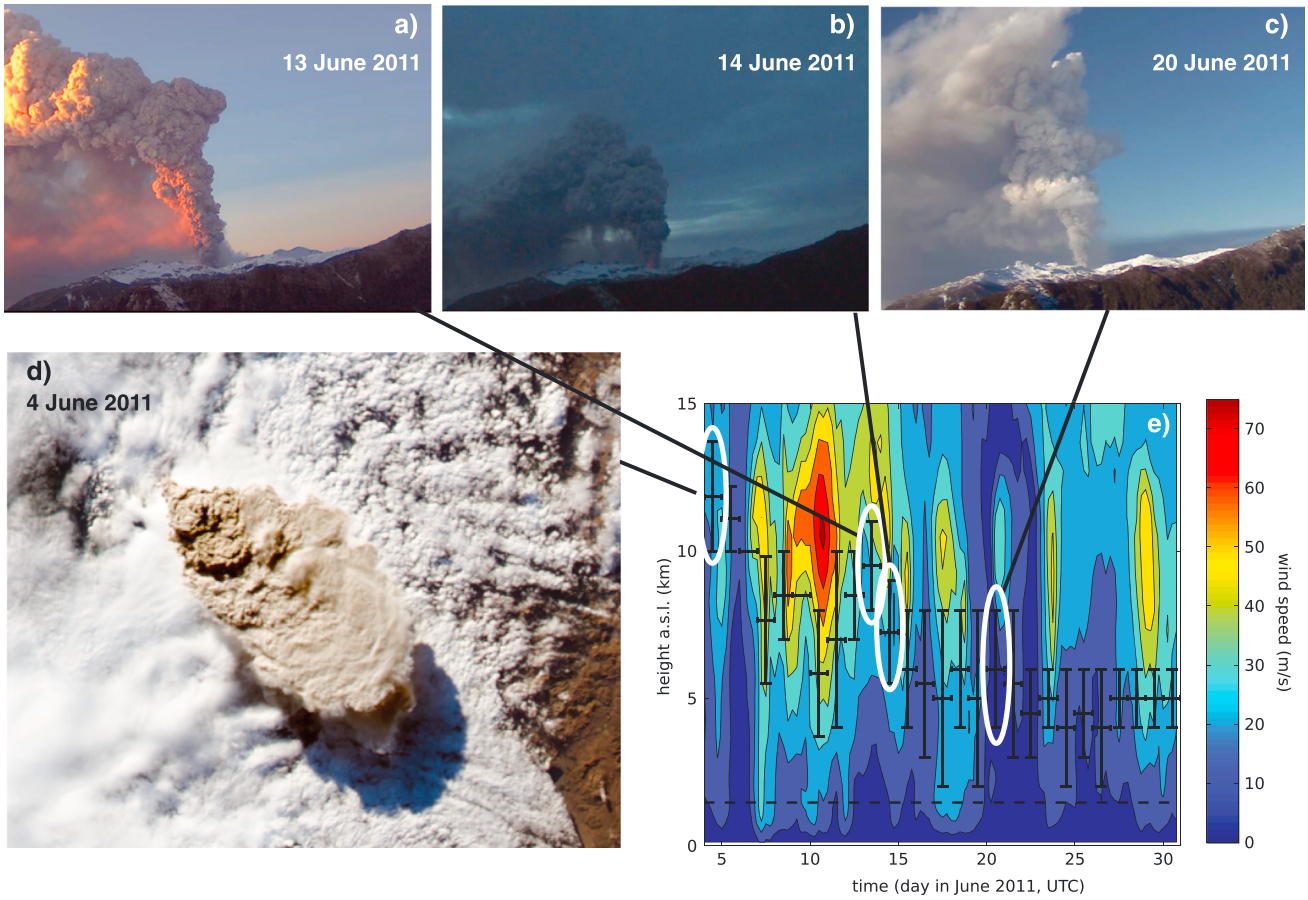

Figure 5. Examples of plumes taken from the Futangue stationary camera on (a) 13, (b) 14, and (c) 20 June 2011 and (d) Moderate Resolution Imaging Spectroradiometer (MODIS) image of the Aqua satellite captured shortly after the beginning of the eruption on 4 June (http://www.earthobservatory.nasa.gov/NaturalHazards/event.php?id=50859). (e) Variation with time (4–30 June 2011) of plume height above sea level (from GVP) and wind speed (ECMWF). The vertical and horizontal error bars indicate the uncertainty associated with the detection of plume height and with the timing of plume height detection as reported by *Collini et al.* [2013] and GVP, respectively. The horizontal dashed line in Figure 5e is the vent height.

trapezoidal integration (Figure 5 and supporting information). From these, we calculate the average buoyancy frequency across the plume height and the density of the atmosphere at the vent height. For the specific heat capacity of air, we use 998 J kg^{-1} K^{-1} [*Woods*, 1988]. The specific heat capacity and the temperature of the gas-pyroclast mixture at the vent and both the radial and wind entrainment coefficients are uncertain, and we therefore use a range of values. Common eruption temperatures for silica-rich eruptions are between 1118 and 1216 K [*Castro et al.*, 2013; *Jay et al.*, 2014]. The specific heat capacity of the gas-pyroclast mixture is dependent on the eruption temperature. We use the parameterization of *Dufek et al.* [2007] and of *Whittington et al.* [2009] and find a range between 1197 and 1211 J kg^{-1} K^{-1} for the explored temperature range. For the radial entrainment coefficient, we use values between 0.05 and 0.15 [e.g., *Carazzo et al.*, 2008; *Morton et al.*, 1956; *Suzuki and Koyaguchi*, 2010], and for the wind entrainment coefficient, we use values between 0.1 and 1 [e.g., *Briggs*, 1972; *Bursik*, 2001; *Contini et al.*, 2011; *Degruyter and Bonadonna*, 2012; *Devenish*, 2013; *Devenish et al.*, 2010; *Hewett et al.*, 1971; *Huq and Stewart*, 1996; *Mastin*, 2014; *Suzuki and Koyaguchi*, 2013], respectively.

The uncertainty within the observations (i.e., plume height and atmospheric data) does not allow for an accurate estimate of the MFR. Uncertainty is further increased by the uncertainty within model parameters (i.e., entrainment coefficients and eruption source temperature). We demonstrate the large errors that can arise in MFR from the combination of these uncertainties in Figure 6 (see also Figure S4 in the supporting information for a comparison with traditional strategies not accounting for wind entrainment). The uncertainty associated with the height and atmospheric observations (indicated by the blue bars in Figure 6) induces an uncertainty of an order of magnitude to several orders of magnitude. The additional uncertainty

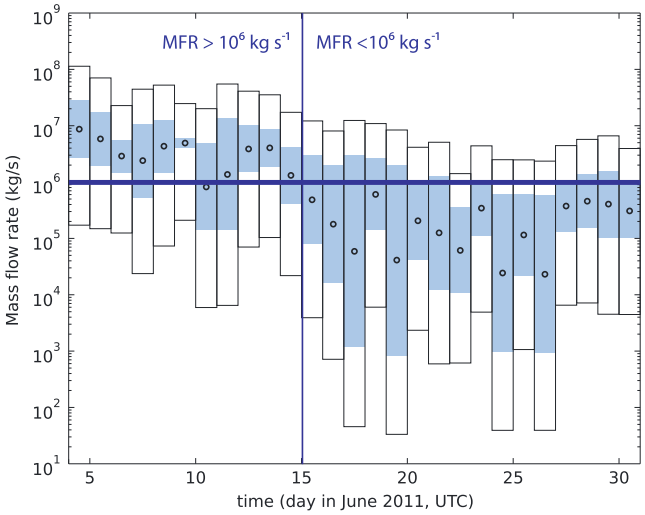

Figure 6. Variation with time (4–30 June 2011) of MFR as determined based on the equation of *Degruyter and Bonadonna* [2012] (equation (1) in the main text). The blue rectangles indicate the variation range of MFR associated with uncertainty on plume height and atmospheric conditions as shown in Figure 5 (radial entrainment, wind entrainment, and eruption temperature were fixed to 0.1, 0.5, and 894°C, respectively). The white rectangles indicate the variation range of MFR including all sources of uncertainty (i.e., using extreme values for height, atmospheric profiles, entrainment rates, and source temperature; see text for details). The black circles indicate the log average of the minimum and maximum values of the blue rectangles. The horizontal blue line indicates the MFR of 10^6 kg s^{-1}.

that stems from the model parameters increases the uncertainty further by several orders of magnitude (indicated by the white bars in Figure 6). In spite of the large uncertainty, we can compare the relative values of the MFR estimates. To this end, we use the log average value of the minimum and maximum MFRs calculated for the observational uncertainty, i.e., the blue bars.

Two main eruptive periods can be distinguished based on MFR values: the first period with largely fluctuating MFR $> 10^6$ kg s^{-1} (between 4 and 14 June; Units I, II, and III) and the second period with MFR $< 10^6$ kg s^{-1} (after 14 June). The highest average MFR was estimated for the climactic phase (i.e., 4 June; layers A and B), i.e., 0.9×10^7 kg s^{-1} (Table 1). This is in agreement with the GVP reports on the eruption, based on the daily bulletins of OVDAS, which describe that eruption started to decrease in intensity by the end of the first day, and with the observed features of the deposits [*Pistolesi et al*., 2015].

The influence of wind entrainment on plume rise was strong throughout the whole eruption, as shown by the distortion of the volcanic clouds toward the wind direction with no obvious upwind spreading (Figure 5). The wind effect on plume rise can be quantified by the ratio of the radial-entrainment and the wind-entrainment terms in equation (1) or, in other words, the ratio of the characteristic time scale for wind entrainment and the characteristic time scale for plume rise in a wind-still environment:

$$\Pi = \frac{\overline{N}H}{1.8\overline{v}}\left(\frac{\alpha}{\beta}\right)^2 \tag{2}$$

Degruyter and Bonadonna [2012] suggested that Π can be used to distinguish between strong ($\Pi \gg 1$) and weak plumes ($\Pi \ll 1$). This has recently been confirmed by laboratory experiments [*Carazzo et al*., 2014]. We define here weak and strong plumes by $\Pi < 0.1$ and $\Pi > 10$, respectively; plumes characterized by $0.1 < \Pi < 10$ are transitional between strong and weak (Figure 7a). *Carazzo et al*. [2014] defined this category as distorted plumes. It is important to stress that the boundary values of 0.01 and 10 for the classification of weak and strong plumes, respectively, are to be considered as indications for comparative analysis more than absolute values, as they strongly depend on the choice of entrainment coefficients. In fact, similar to the MFR, the value of Π can suffer from large uncertainties (e.g., Figure 7b). The difference here is that the observational uncertainty from height and atmospheric data is quite small and allows estimating Π within an order of magnitude or less. The additional uncertainty within the entrainment coefficients, however, creates a very large uncertainty of several orders of magnitude. As in the case of the MFR, we use the log average value of the minimum and maximum MFRs calculated for the observational uncertainty, i.e., the blue bars, to relatively compare differences in the influence of wind.

Throughout the whole eruption, the characteristic time for wind entrainment is faster than the time scale for rise in a wind-still environment, i.e., $\Pi < 1$, and thus, the contribution of wind is significant. In particular, Π fluctuates between 0.02 and 0.17 (black circles in Figure 7b) and does not correlate with MFR. In fact, while MFR quantifies the eruption intensity, Π quantifies the plume interaction with the atmosphere. This is most prominently demonstrated by the periods of 4–6 June and 20–22 June that are both associated with

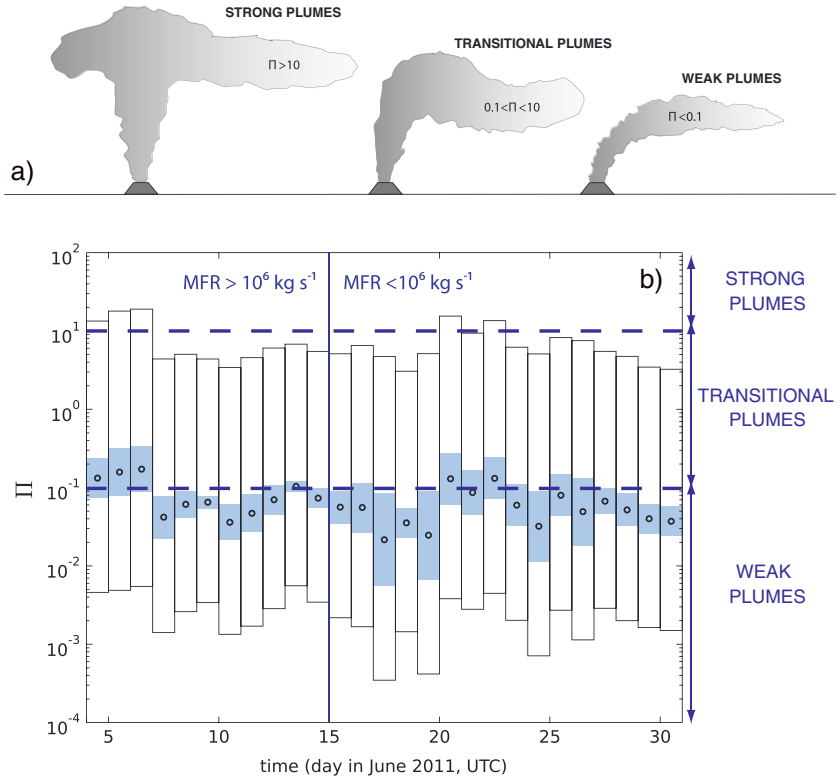

Figure 7. (a) Simplified sketch illustrating strong, transitional, and weak plumes based on the scaling parameter Π and (b) variation of Π with time as determined with the equation of *Degruyter and Bonadonna* [2012] (equation (2) in the main text). See caption of Figure 6 for the descriptions of symbols. The horizontal blue dashed lines indicate the fields of strong ($\Pi > 10$), transitional ($0.1 < \Pi < 10$), and weak plumes ($\Pi < 0.1$), respectively. The vertical blue line indicates the transition between the periods characterized by MFR $>$ and $< 10^6$ kg s^{-1}.

transitional plumes (i.e., $0.1 < \Pi < 10$), indicating that wind is significant but not dominating the plume rise height (Figures 5c and 5d and Figure 7). However, these periods can be distinguished by a high intensity (MFR $> 10^6$ kg s^{-1}) for the first period but a low intensity (MFR $< 10^6$ kg s^{-1}) for the latter period. The periods of 7–12, 14–19, and 23–30 June were characterized by weak plumes ($\Pi < 0.1$), for which wind is the controlling factor of the plume height (Figures 5 and 7). They were also of varying intensity (Figure 7). To give additional insight into the meaning of Π, we use it to estimate how much the effective height of the plume is reduced compared to the height the plume would have reached if it is rising in a wind-still environment (termed *H_nowind*). Using equation (1), we find that

$$\frac{H}{H\_nowind} = \left(\frac{1}{1+\left(\frac{1}{\Pi}\right)}\right)^{\frac{1}{4}} \tag{3}$$

For the days with the highest Π (i.e., 0.1–0.2; i.e., 4–6 and 20–22 June), the actual plume height *H* is between 55% and 64% of *H_nowind*, while for the days with the lowest Π (i.e., 0.02–0.05), *H* is between 37% and 47% of *H_nowind*.

3.4. Eruption Duration

Based on the evaluation of the average MFR with time (Figure 6) and the estimated erupted mass for each phase as reported in Table 1, an approximate duration of each phase was determined and compared with data derived from direct observation. In particular, layers A–B, A–F, H, and K2 resulted to be associated with a mean duration of 5.1, 17.2, 8.3, and 3.2 h, respectively (Table 1). Durations of the sustained phases are likely to be longer if we consider the estimated erupted mass as minimum values due to the intrinsic uncertainty associated with the volume calculations based on both empirical fitting and analytical inversion [*Bonadonna and Costa*, 2012] and the calculated MFR as associated to maximum values of plume height as

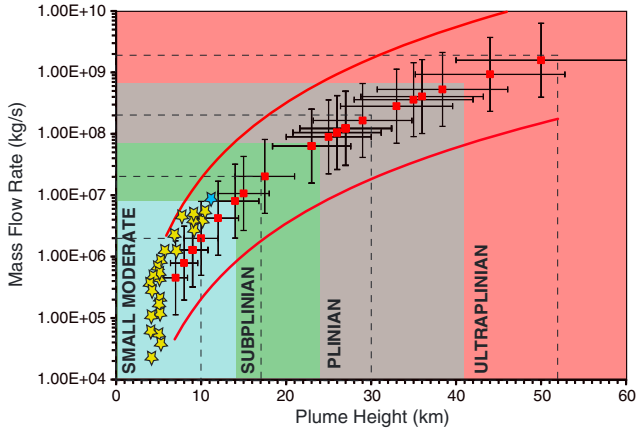

Figure 8. Classification of the Cordón Caulle eruption based on the plume height versus MFR plot of *Bonadonna and Costa* [2013a] showing a combination of subplinian (blue star; 4 June 2011) and small-moderate plumes (yellow stars; 5–30 June 2011) of the Cordón Caulle eruption. Plume height is indicated as the average of observations above the vent (kilometer), and MFR is calculated based on the model of *Degruyter and Bonadonna* [2012] (black circles in Figure 6). All MFR estimates are within a factor of 10 (red solid lines) from *Mastin et al.*'s [2009] estimates (red squares). The horizontal and vertical error bars on the red squares indicate a typical 20% error on the calculation of plume height and a typical MFR spreading of a factor of 4 as indicated by *Mastin et al.* [2009], respectively.

reported by both *Collini et al.* [2013] and GVP (Table 1). In addition, the determination of plume height can be associated with significant uncertainties even for recent eruptions [*Oddsson et al.*, 2012; *Prejean and Brodsky*, 2011; *Tupper and Wunderman*, 2009]. Considering the fourth-power relation between MFR and plume height (equation (1)), even small uncertainties in plume height measurements could result in large MFR uncertainties and therefore duration uncertainties. The uncertainty in MFR from both plume height observations and atmospheric conditions (blue bars in Figure 6) for the 4–6 June (20–30%) and 7 June (50%) events results in an even larger duration uncertainty, i.e., 85–95% (Table 1 and supporting information). Additional sources of uncertainty stem from the model assumptions, such as entrainment coefficients and eruption temperature (white bars in Figure 6). However, considering the good agreement between eruption duration derived from MFR analysis and duration of the various eruption phases as observed from satellite images (i.e., 24–30 h for layers A–F and $<$12 h for layers H and K2 [*Pistolesi et al.*, 2015]), we suggest that both eruptive and atmospheric conditions did not vary significantly within each of the studied phases.

3.5. Eruption Classification

Given the complexity of characterizing and classifying long-lasting eruptions, here we consider both individual and cumulative phases and discuss the resulting implications. The phases A–F of the Cordón Caulle eruption could be classified based on erupted volume/mass, MFR, plume height, thickness, LL, and Mdϕ data. In particular, a total volume/mass of 0.80 ± 0.17 km^3/$4.5 \pm 1.0 \times 10^{11}$ kg results in a VEI 4 [*Newhall and Self*, 1982] and a magnitude of 4.6 [*Pyle*, 2000] (Table 1). Based on the MFR versus plume height classification of *Bonadonna and Costa* [2013a], only the plume developed on 4 June can be classified as subplinian, whereas all other plumes plot in the field of small-moderate eruptions (Figure 8). The classification plot based on Weibull thickness and LL parameters for layers A–F results in small-moderate eruptions transitional to subplinian, whereas Weibull parameters of thickness versus Mdϕ result in clear small-moderate eruptions [*Bonadonna and Costa*, 2013a] (Figure 9). Finally, given that the thinning trend of layers A–F can be described by three exponential segments on a log(thickness) versus the square root of area [*Pistolesi et al.*, 2015], three values of b_t can be obtained (i.e., 2.9, 8.3, and 24.4 km) and therefore three values of ratio b_c/b_t (i.e., 2.8, 1.0, and 0.3 for the isopleth map of Figure 2a), with b_t and b_c being the distance over which the maximum thickness and the size of the largest clast decrease by half, respectively [*Pyle*, 1989]. These parameters plot in the field of plinian to ultraplinian eruptions in the classification scheme of *Pyle* [1989]. Given the available data set, the phases A and B (0.28 ± 0.15 km^3), H (0.21 ± 0.07 km^3), and K2 (0.05 ± 0.01 km^3) could only be classified based on erupted volume and mass and can be associated with VEIs 4 (layers A and B and H) and 3 (layer K2) and magnitudes 4.2 (layers A and B), 4.1 (layer H), and 3.4 (layer K2), respectively (Table 1).

4. Cloud Spreading

When they reach the level of neutral buoyancy, vigorous plumes start spreading as gravity currents as they are denser at their top and less dense at their base than the surrounding stratified atmosphere, and their crosswind

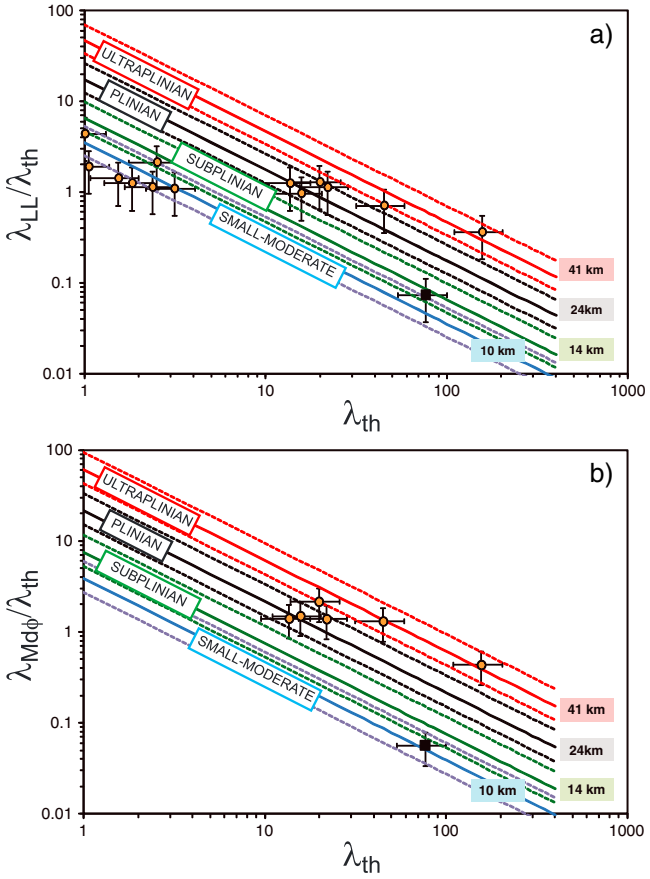

Figure 9. Classification of the Unit I (A–F cumulative layer; black squares) based on the Weibull fit for (a) thinning versus largest clast trend (λ_{th} and λ_{LL}) and (b) thinning versus Mdϕ trend (λ_{th} and $\lambda_{Md\phi}$) (adjusted from *Bonadonna and Costa* [2013a]). The red, black, green, and blue solid lines represent theoretical lines for Ht of 41, 24, 14, and 10 km based on the empirical equations of λ_{LL} and $\lambda_{Md\phi}$ versus plume height for Figures 9a and 9b, respectively. The dashed lines indicate a 20% error in the calculation of plume height. The error bars of 30, 50, and 40% are also shown for the estimation of λ_{th}, $\lambda_{LL}/\lambda_{th}$, and $\lambda_{Md\phi}/\lambda_{th}$, respectively (as taken from *Bonadonna and Costa* [2013a]). Examples of plinian to ultraplinian (i.e., Taupo, Hatepe, Tarawera, Cotopaxi layer 3, Cotopaxi layer 5, and Pululagua) and subplinian to small-moderate eruptions (i.e., Vesuvius 512, Averno A1 to A6, and Boqueron C) are also shown (orange circles; see *Bonadonna and Costa* [2013a] for more details).

spreading is proportional to the volumetric flow rate at the neutral buoyancy level [e.g., *Sparks et al.*, 1997]. As a result, higher plumes would spread laterally more rapidly than lower plumes such that [*Bonadonna and Phillips*, 2003]

$$w = \frac{2x}{1 + a\sqrt{x}} \tag{4}$$

with $a = \frac{u}{\sqrt{\lambda NQ/\varepsilon}}$, where w is the crosswind width (m); x is the downwind distance (m); u is the wind velocity at the neutral buoyancy level (m s^{-1}); Q is the volumetric flow rate at the neutral buoyancy level (m^3 s^{-1}), which we determined with the 1-D model of *Degruyter and Bonadonna* [2012] (supporting information); N is the atmospheric buoyancy frequency (s^{-1}) assumed to be 0.01 s^{-1} for these calculations as all plumes developed in the troposphere; λ is a constant of the order of unity that depends on flow geometry and ambient stratification (here 0.8); and ε is a geometrical perimeter factor assumed to be 3.9 (with an uncertainty on the calculated cloud width of 25%; see *Bonadonna and Phillips* [2003] for more details). In contrast, plumes that are strongly affected by wind maintain the vorticity structure characteristic of the convective column also when they reach their maximum height and start spreading horizontally [*Sparks et al.*, 1997]. Their crosswind spreading at the neutral buoyancy level is typically described by turbulent diffusion (i.e., Fickian diffusion) such that [*Bursik*, 1998]

$$w = 4\sqrt{\frac{Kx}{u}} \tag{5}$$

where K is the horizontal eddy diffusivity, i.e., diffusion coefficient (m^2 s^{-1}). We have already shown how the plumes developed on 4 and 6 June were transitional between weak and strong plumes. Downwind (distance from vent) and crosswind (width) distances and velocities were calculated from GOES images for the cloud developed on both days in order to establish the relative contribution of gravitational spreading (Figure 10). A significant wind shift is evident on 6 June, with the cloud first spreading toward NE and then moving SE and toward the Atlantic Ocean. Due to the constraint of satellite images, the spreading of the SE cloud on 6 June could not be analyzed. Width and downwind length of the isomass maps of layers A–F deposit (i.e., Unit I—4 and 5 June; supporting information) were also investigated and compared with the cloud geometry.

The best fit is given by the linear combination of gravity spreading and turbulent diffusion following *Bursik* [1998], with a diffusion coefficient of 9000 m^2 s^{-1} for both days (Figure 11a). The observed crosswind width lays

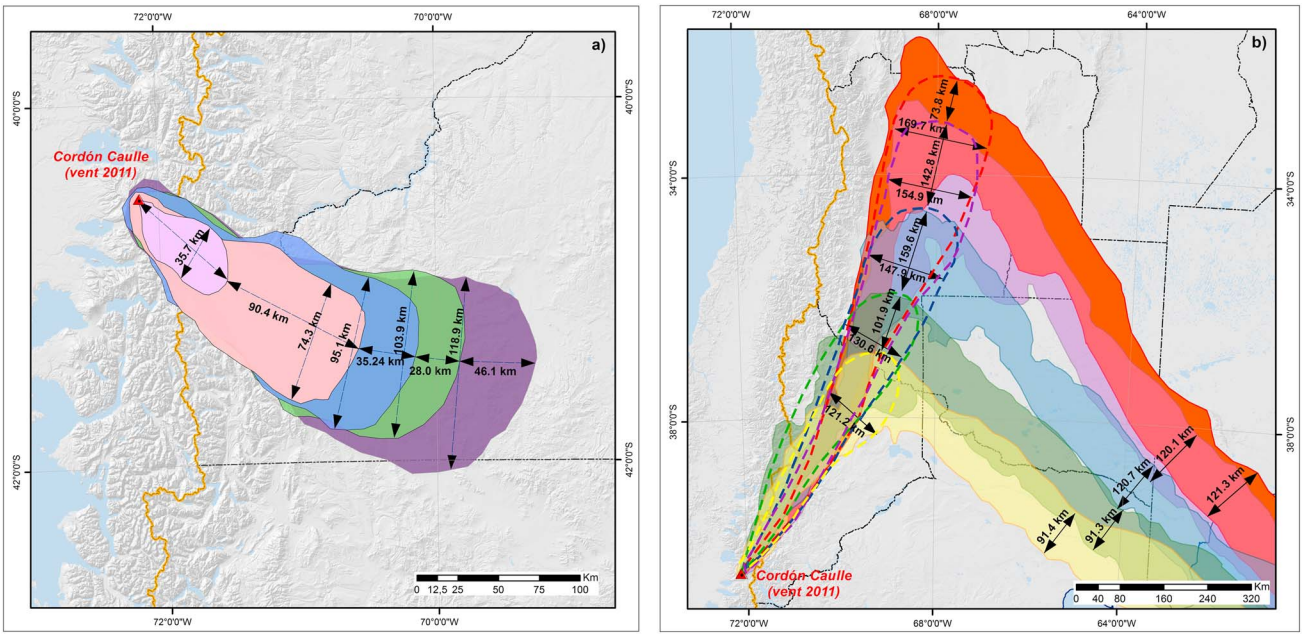

Figure 10. Downwind and crosswind extensions of the volcanic clouds developed on (a) 4 June 2011 and (b) 6 June 2011 as observed from the GOES satellite images for the time interval of 18:45–20:15 UTC and 12:45–19:45 UTC, respectively (total measurement uncertainty includes pixel size of these GOES images, i.e., ~2 km and definition of cloud boundaries, i.e., ~5 km). On 6 June, two distinct clouds developed: one moving toward NE and one moving toward SE.

in between the linear combination of gravitational spreading and turbulent diffusion for the minimum and maximum observations of volumetric flow rate (solid and dashed lines in Figure 11a). The range of volumetric flow rate depends on the uncertainty on both plume height and atmospheric conditions (see Figure 5e). Radial entrainment, wind entrainment, and eruption temperature were fixed to 0.1, 0.5, and 1167 K, respectively. The dispersal of the 1 kg m^{-2} isoline of Unit I (deposited on 4 and 5 June) can also be described by the linear combination of gravity spreading and turbulent diffusion (Figure 11a). Relative contribution of the gravitational spreading is 49–71% and 40–50% for minimum and maximum volumetric flow rates on 4 and 6 June, respectively, with no significant variation with distance from vent (standard deviation $<$2%). Results for equation (5) (Fickian diffusion; Figure 11b) and equation (4) (gravitational spreading; Figure 11c) have also been plotted separately. Fickian diffusion seems to be able to describe the cloud spreading of both 4 and 6 June but only if unrealistic values of diffusion coefficients are considered (i.e., 90,000 and 30,000 m^2 s^{-1}, respectively), which are higher than the range expected for atmospheric dispersion over brief time intervals (10–10^4 m^2 s^{-1} [*Heffter*, 1965; *Pasquill*, 1974]). Finally, pure gravitational spreading seems to underestimate the observed cloud spreading for both days, with the largest discrepancies being associated with the 6 June event (Figure 11c).

The downwind and crosswind velocities of the cloud were calculated based on the distance from vent and from the central axis, respectively, as observed from GOES images in Figure 10 and the associated observation times (Figure 12). The downwind velocity is higher than the associated wind velocity at the neutral buoyancy level, and such a discrepancy is due to the contribution of the gravitational component to plume spreading. The velocity due to gravitational spreading, u_b, was calculated with the equation of *Bonadonna and Phillips* [2003]:

$$u_b = \sqrt{\frac{\lambda N Q}{\varepsilon x}} \tag{6}$$

which is equivalent to equation (10) of *Costa et al.* [2013]. Our results show that for both plumes considered (i.e., 4 and 6 June), the crosswind velocity can be well described by a lateral spreading due to buoyancy, while the downwind velocity can be described by a linear combination of wind advection and gravitational spreading (Figure 12). In particular, the crosswind velocity of 4 June is between 6 and 10 m s^{-1}, while the crosswind velocity of the NE cloud of 6 June is between 1 and 2 m s^{-1}. As a comparison, the crosswind velocity of the SE cloud of 6 June is between 0 and 1 m s^{-1}. Downwind velocity of 4 and 6 June (NE cloud) is between 35–45 m s^{-1} and 17–21 m s^{-1}, respectively. Relative errors between observed and calculated

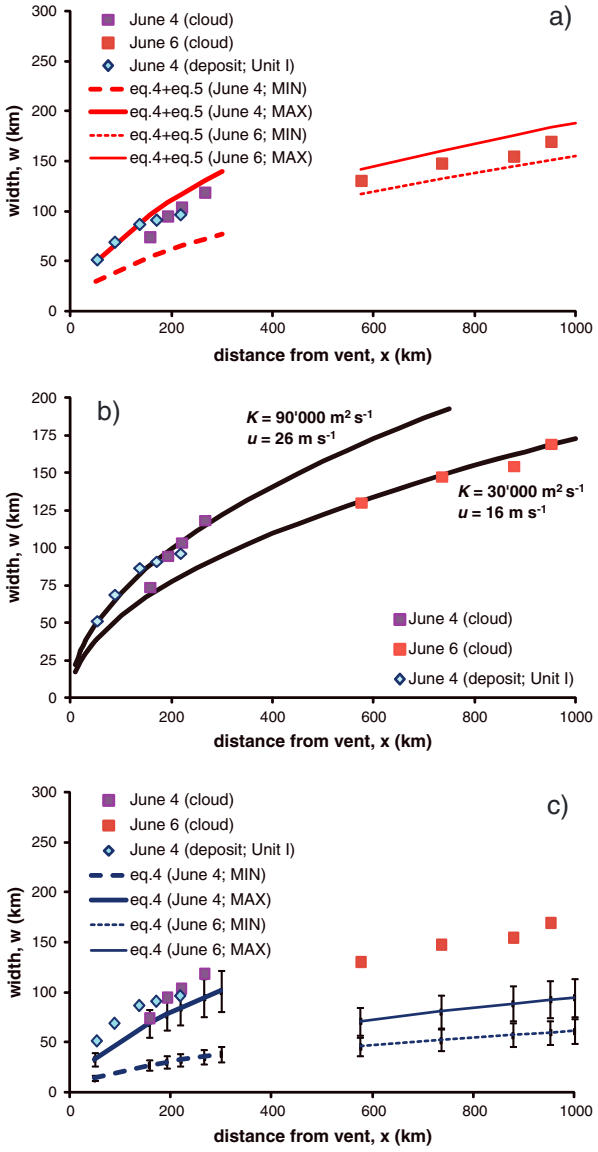

Figure 11. Variation of downwind distance from vent versus width for (i) volcanic clouds developed on both 4 and 6 June (NE cloud) as observed from satellite images (violet and red squares, respectively; from Figure 10) and (ii) 1 kg m^{-2} isoline of Unit I (blue diamonds; supporting information) described as (a) gravitational spreading plus turbulent diffusion (for a best fit diffusion coefficient of 9000 $m^2 s^{-1}$). The dashed and solid lines are associated with minimum and maximum values of volumetric flow rate (Q) at the neutral buoyancy level, respectively, related to variable plume height and atmospheric conditions, i.e., $0.5–4.3 \times 10^9$ $m^3 s^{-1}$ (for the 4 June event) and $3.5–8.6 \times 10^8$ $m^3 s^{-1}$ (for the 6 June event) (as calculated with the model of *Degruyter and Bonadonna* [2012]); (b) turbulent diffusion (equation (5)) for best-fit diffusion coefficients K ($m^2 s^{-1}$) and wind velocity u ($m s^{-1}$) averaged between neutral buoyancy level and total plume height and between the volcano location and the maximum extension of the observed cloud for 4 and 6 June (indicated next to best fit lines); for simplicity, an average wind velocity of 29 m s^{-1} for minimum and maximum plume heights of 4 June was considered; and (c) gravitational spreading (equation (4) considering $\lambda = 0.8$ and $N = 0.01$ s^{-1}; see *Bonadonna and Phillips* [2003] for more details). The vertical bars indicate a 20% uncertainty on the calculated width in relation to the cloud geometry (see *Bonadonna and Phillips* [2003] for more details).

downwind velocity are <7% for 4 June and <13% for 6 June. The distal increase in downwind velocity for both 4 and 6 June seems to be mostly related to a local increase in wind velocity.

5. Discussion

The 2011 eruption of Cordón Caulle, together with the 2008–2009 eruption of Chaitén (Chile), represents rare cases of rhyolitic eruptions that have been witnessed and studied in detail. They were both long lasting and caused widespread disruption to various economic sectors and transport systems, mostly in Argentina due to the prevailing westerly winds that characterize the middle latitudes. The associated large amount of airborne ash caused major disturbance to aviation in Argentina, and to a lesser extent, in Australia and New Zealand that, however, was not as severe as in Europe during the 2010 Eyjafjallajökull eruption only due to less dense air traffic [e.g., *Collini et al.*, 2013; *Folch et al.*, 2008]. In addition, *Castro and Dingwell* [2009] showed how, regardless of the high silica content, rhyolitic eruptions can develop quickly, most likely because they are associated with shallow magma chambers [*Wicks et al.*, 2011] that often exist at near-liquidus, hydrous magmatic conditions. Consequently, rhyolitic magmas may have lower viscosities than expected [*Castro et al.*, 2013; *Jay et al.*, 2014] and are therefore highly mobile. As a result, a detailed account of physical parameters, such as erupted mass, MFR, plume height, and eruption duration constrained in this study (Table 1) in combination with total grain size distribution [*Bonadonna et al.*, 2015], and their variation with time is particularly important to forecast future eruptions and mitigate the associated risk. In addition, the eruptive dynamics of long-lasting small-moderate eruptions, such as that of Cordón Caulle, are complicated

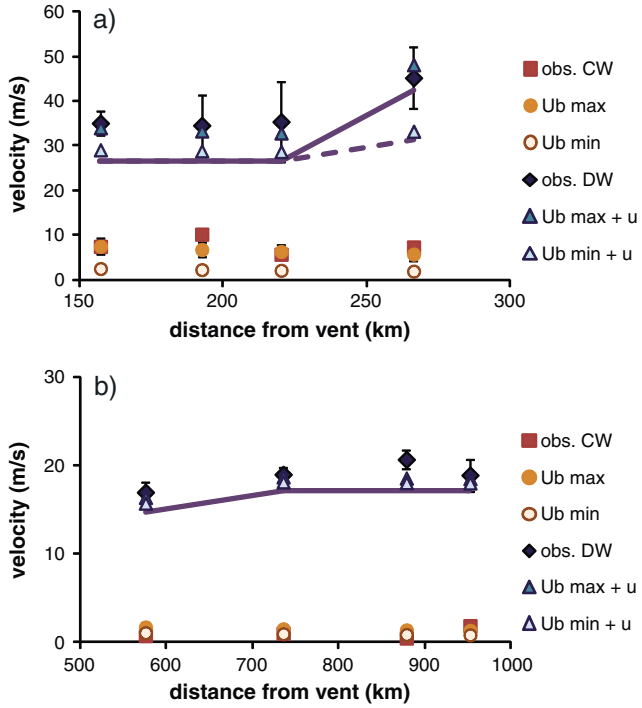

Figure 12. Variation of spreading velocity in the downwind (blue diamonds) and crosswind (red squares) directions at various distances from vent for (a) 4 June 2011 (observations between 18:45 and 20:15 UTC) and (b) 6 June 2011 (observations between 12:45 and 19:45 UTC). The solid and dashed lines indicate the wind velocity u (m s^{-1}) at each distance from vent for minimum and maximum plume heights (see Figure 5 and supporting information for plume height data; only one height observation is available for 6 June). Wind data are averaged between the neutral buoyancy level and total plume height for each cloud position. The circles and triangles indicate, respectively, the spreading velocity due to buoyancy (u_b, as calculated for minimum and maximum values of Q from equation (6) considering $\lambda = 0.8$ and $N = 0.01$ s^{-1}) and the downwind velocity calculated as a combination between u_b and u. Q values used in equation (6) are described in the caption of Figure 11. The vertical bars indicate the uncertainty associated with the observed velocity derived from an average cumulative error of ±7 km on the downwind and crosswind lengths (see Figure 10 for more details). A 25% uncertainty on the calculated minimum and maximum cloud-spreading velocities due to buoyancy (u_b) is also shown (as estimated by *Bonadonna and Phillips* [2003] in relation to the cloud geometry).

by the interaction with the variable atmospheric and source conditions, which make the characterization of the physical parameters and the classification of the eruption more challenging than for short powerful eruptive events.

5.1. Eruption Classification

Due to its long-lasting character and the variation of eruptive parameters through time, the 2011 Cordón Caulle eruption represents a typical example of an eruption that can be classified with different eruptive styles depending on the strategy used and the section of the deposit considered. The MFR versus height plot suggested by *Bonadonna and Costa* [2013a] shows the transitional character from subplinian to small-moderate eruptions for the different eruptive phases, also confirmed by the Weibull parameters fitting the LL and Mdϕ trends. The classification of small-moderate eruptions based on the Mdϕ plot (Figure 9), as opposed to transition between small-moderate and subplinian, can be explained with Mdϕ values being slightly underestimated due to breakage of the most abundant variable density juvenile clasts and the constant presence of a fine-grained subpopulation which tends to decrease the Mdϕ value [*Bonadonna et al.*, 2015]. Conversely, the use of the exponential parameters b_t and b_c/b_t of *Pyle* [1989] is made complex by the presence of multiple segments in the log(thickness) versus square root of isopach area diagram of layers A–F and therefore multiple values.

Finally, it is important to discuss the application of the VEI and magnitude scale to long-lasting eruptions with different eruptive styles [e.g., *Siebert et al.*, 2010]. VEI and magnitude values vary depending on the eruptive phases considered in the calculation. If individual phases/layers are considered, VEI and magnitude values range between 3 (layer K2)–4 (layer H) and 3.4 (layer K2)–4.1 (layer H), respectively. However, if the cumulative tephra deposits of layers A–F or A–F + H + K2 are considered (i.e., 4 June and the period between 4 and 15 June 2011, respectively), VEIs 4 and 5 and magnitudes 4.6–4.8 are obtained, respectively. It is clear in this case that any correlation between VEI and eruption intensity (i.e., column height) implicit in the VEI formulation is not correct. Unfortunately, individual layers A to F could not be distinguished through the whole deposit, and therefore, associated volume could not be calculated. It is often the case that individual layers of long-lasting eruptions cannot be easily distinguished in the field and the volume of cumulative deposits represents the only available information. One should also bear in mind that VEI and magnitude values of cumulative deposits of short- and long-lasting eruptions cannot be directly compared, above all when durations are

significantly different (e.g., a few hours versus a few days/weeks/months). It is also important to consider that the VEI values calculated for Cordón Caulle do not include the volume of associated PDCs, even though in the original interpretation by *Newhall and Self* [1982], VEI should be based on the total volume of ejecta (i.e., both tephra and PDC material).

5.2. Mass Flow Rate, Erupted Mass, and Eruption Duration

The importance of the wind entrainment on the calculation of the MFR is shown in Figure 6, with discrepancies with traditional strategies up to 1 order of magnitude (see also Figure S4 in the supporting information). Our results also show that due to the interaction with variable atmospheric conditions, plumes with similar height could be associated with different MFR values. As an example, plumes developed on 27–30 June have similar heights, or even lower, than the plumes developed on 22–26 June but are characterized by higher MFR values (i.e., $3.0–4.6 \times 10^5$ kg s^{-1} and $0.2–3.4 \times 10^5$ kg s^{-1}, respectively; Figures 5e and 6). *Collini et al*. [2013] also accounted for the effects of wind on plume rise but, for the period of 4–19 June 2011, obtained lower values of average MFR (i.e., 1.7×10^6 kg s^{-1}) and higher values of erupted mass (i.e., 2.4×10^{12} kg). These values are nearly half of the average MFR derived from the analytical equation of *Degruyter and Bonadonna* [2012] for the 4–19 June period, i.e., 3.3×10^6 kg s^{-1}, due to a different choice of plume height values and model assumptions that are most likely related to the radial and wind entrainment coefficients. However, the total erupted mass of *Collini et al*. [2013] is larger than our values (i.e., $6.0 \pm 1.1 \times 10^{11}$ kg, as averaged between empirical integration and inversion strategies) probably because the authors have assumed a daily constant MFR throughout the whole eruption. These discrepancies show the complexity and high uncertainty associated with the characterization of even recent and observed volcanic eruptions, confirming the importance of combining detailed field studies with modeling strategies.

It is important to mention the complex application of inversion strategies to both layers A and B and A–F, which does not result in well-constrained solutions even for the erupted mass (Figure 4). Such a complexity cannot be related to the presence of a large mass of fine ash (the $\geq 3\ \phi$ fraction being smaller than ~15% of the total deposit) but is most likely due to the strong advection of the eruptive column and the combination of multiple thin layers indicative of a long-lasting pulsating activity difficult to be captured by semianalytical models such as TEPHRA2. Only well-targeted inversion runs provide results in agreement with observations. The calculations of the erupted mass and MFR are in broad agreement with the observed duration of ~27 h of *Jay et al*. [2014] and 24–30 h of *Pistolesi et al*. [2015] (i.e., duration between 6 and 54 h; Table 1). Conversely, if the erupted mass associated with the first phase (Unit I) is divided by the observed duration of ~27 h, an average MFR of 4.6×10^6 kg s^{-1} is found. This is in agreement with the average of the minimum MFR values calculated with the analytical equation of *Degruyter and Bonadonna* [2012] for the first 2 days (i.e., 2.3×10^6 kg s^{-1}).

5.3. Wind Effect on Plume Dynamics

Deposit features associated with the first phase of the eruption (Unit I) suggest sedimentation from a plume strongly affected by wind advection. All maps describing the tephra deposits are strongly elongated, i.e., isopleth maps of both LL and Mdφ (Figures 2 and 3) and isomass maps of both total deposit and individual size categories (supporting information and *Bonadonna et al*. [2015]). It is interesting to note how even the 1.6 cm contour for both isopleth maps is elongated downwind (Figure 2), indicating that both the rising plume and the umbrella cloud were significantly affected by the wind, as also visible from the satellite images (Figure 5d). *Bursik et al*. [1992] and *Volentik et al*. [2010] have shown how the 1.6 cm clasts are transitional between sedimentation from plume margins and sedimentation from umbrella cloud for plume heights between 21 and 36 km (i.e., Fogo A (Azores) and Pululagua 2450 B.P. (Ecuador)). Considering the significantly lower plume of the 2011 Cordón Caulle eruption, we expect the 1.6 cm clasts to fall out before reaching the neutral buoyancy level. In case of a vertical plume, the 1.6 cm contour should have been concentric around the vent, as shown by the isopleths of vigorous plumes (e.g., Fogo A [*Walker and Croasdale*, 1971] and Novarupta 1912 [*Fierstein and Hildreth*, 1992]). In addition, all isopleth contours suggest a wind speed at the tropopause of ~40 m s^{-1} as derived with the method of *Carey and Sparks* [1986]. However, ECMWF wind data show lower wind velocities at the tropopause (i.e., ~11 km above sea level) than derived from the model of *Carey and Sparks* [1986] for 4 and 5 June (i.e., 10–30 m s^{-1}) and very strong winds for 7–11 June (30–80 m s^{-1}) (Figure 5). This is probably related to the fact that the vertical velocities of Cordón Caulle plumes are lower than

the typical plinian plume velocity considered in the model of *Carey and Sparks* [1986], and caution is called in applying the model for the deposits of this type of eruptions.

Our results demonstrate that plume height is not always a good indicator of eruptive conditions at the vent as it is strongly controlled by the interaction with the surrounding atmosphere. The scaling parameter Π incorporates these effects and can be used to discriminate between strong, transitional, and weak plumes (Figure 7). This parameter is independent of the MFR as is demonstrated by the occurrence of both transitional and weak plumes in the high- and low-MFR periods (Figures 5, 6, and 7). A careful analysis of the influence of the wind on plume height has shown that wind is dominant in controlling the rise height over the buoyancy by factors of 6–46 throughout the whole month of June and by factors of 6–8 during the first 2 days of the eruption (Unit I) (Π of 0.16–0.02 and 0.16–0.13, respectively; Figure 7b and supporting information). This is particularly clear in the MODIS image of the first few hours of the eruption that show no upwind cloud spreading (Figure 5d) and in the GOES images of the following hours, showing a very limited upwind spreading with a stagnation point not farther than 5–10 km from the vent vertical (Figure 10a). Wind, thus, has an important first-order effect on the plume height and needs to be accounted for when it is being used to invert for eruption source parameters. This effect will be strongest for weak plumes, such as the ones produced during certain periods of the 2010 Eyjafjallajökull and the 2011 Cordón Caulle eruptions (minimum $\Pi = 0.02$ for both eruptions [*Degruyter and Bonadonna*, 2012]), but can also be significant for transitional plumes. Examples of transitional plumes are those associated with certain periods of both the 2010 Eyjafjallajökull and the 2011 Cordón Caulle eruptions (maximum $\Pi = 0.18$ and 0.17, respectively [*Degruyter and Bonadonna*, 2012]) and those of the Mount St. Helens 1980 eruption ($0.2 < \Pi < 0.34$ [*Carazzo et al*., 2014; *Degruyter and Bonadonna*, 2012]).

SERNAGEOMIN reported numerous PDCs at the beginning of the eruption (at least five in the first 2 days), as well as at the onset of the (weaker) second eruptive period (after 14 June). Between 6 and 13 June, much fewer PDCs were reported (e.g., GVP; http://www.volcano.si.edu). Quantities involved in plume collapse, such as initial density difference, vent radius, exit velocity, and overpressure, will affect this behavior [*Valentine and Wohletz*, 1989], but MFR calculations suggest fairly constant source conditions during this period. The 6–13 June period is characterized by particularly strong winds (Figure 5e), which could increase the plume buoyancy due to entrainment of air by wind shear and limit the formation of PDCs [*Degruyter and Bonadonna*, 2013].

5.4. Cloud Spreading

Crosswind spreading of the clouds associated with the transitional plumes developed on 4 and 6 June could be best described by the linear combination of gravitational spreading and turbulent diffusion with values of diffusion coefficients similar for both days (i.e., 9000 $m^2 s^{-1}$) that are significantly higher than those observed for low-energy bent-over plumes advected as lenses of aerosol and gas with nearly constant width (e.g., ~10 $m^2 s^{-1}$ for Mount Augustine eruption, 3 April 1986 [*Sparks et al*., 1997; *Bursik*, 1998]) but are in the range of observed horizontal diffusivity over brief time intervals (10–10^4 $m^2 s^{-1}$ [*Heffter*, 1965; *Pasquill*, 1974]). Contrary to the 1996 Ruapehu eruption for which the deposit was wider than the cloud, both cloud spreading and deposit during the first couple of days of the Cordón Caulle eruption seem to be characterized by similar crosswind dispersal (Figure 11). In addition, the Ruapehu clouds clearly spread at a similar velocity as the wind at the neutral buoyancy level [*Bonadonna et al*., 2005a], while the downwind velocity of the clouds developed during the Cordón Caulle eruption can be better described by a linear combination of gravitational spreading and wind advection. Discrepancies between calculated and observed values of downwind velocity are <15%, which are mostly within the uncertainty related to geometry assumptions (Figure 12).

In order to distinguish between passive transport by wind and gravitational spreading, *Costa et al*. [2013] defined the cloud Richardson number ($Ri \approx {u_b}^2/u^2$), whereby $Ri < 0.25$ indicates a cloud spreading dominated by wind advection, and for $Ri > 1$, the transport is density driven. In the case of the Cordón Caulle eruption, we find an average Ri~0.01–0.05 on 4 June and ~0.003–0.01 on 6 June, which would suggest that only passive transport plays a role. However, our results suggest that the downwind velocity can be described by $u_b + u$ (Figure 12). In this case, the fraction contributed by gravitational spreading is easily quantified by $u_b/(u_b + u)$, which, in terms of Ri, becomes $1/(1 + 1/\mathrm{sqrt}(Ri))$. We find that the fraction of gravitational spreading contributes between 8–19% and 5–9% of the total spreading for 4 and 6 June,

respectively. This suggests that gravitational spreading can be relevant for *Ri* down to 0.003, but that for low *Ri*, it cannot be the only transport mechanism (i.e., complementary mechanisms being, for example, wind advection and turbulent diffusion). This explains, for example, why the crosswind spreading can be described by a linear combination of gravitational spreading and turbulent diffusion and not by gravitational spreading only (Figure 11). The decrease with distance from the vent of the relative contribution of the gravitational spreading to the total cloud spreading cannot be appreciated at the range of observed distances (150–300 km and 600–950 km for 4 and 6 June), as it remains constant between 49–71% and 40–50% associated with minimum and maximum volumetric flow rates of 4 and 6 June, respectively (standard deviation $<2\%$).

We suggest that, even for low Richardson number and low MFR, cloud downwind velocity of the Cordón Caulle eruption was characterized by an important gravitational component at least during the first few days (4–6 June), and the crosswind spreading (i.e., cloud width) can be described by a linear combination of both gravitational spreading and turbulent diffusion, with diffusion coefficients that are more consistent with observations (i.e., ~9000 $m^2 s^{-1}$) (Figures 11 and 12). This suggests that gravitational spreading, already shown to be crucial to cloud development of strong plumes (e.g., Mount St. Helens 1980 [*Bonadonna and Phillips*, 2003], Pinatubo 1991 [*Costa et al*., 2013], and plinian supereruption at Yellowstone volcano [*Mastin et al*., 2014]), seems to describe also medial-to-distal spreading (100–1000 km) of plumes characterized by relatively low MFR (10^6–10^7 kg s^{-1}).

6. Conclusions

Based on our detailed field campaigns and analytical studies, we can conclude that

1. The 2011 Cordón Caulle eruption started on 4 June and was characterized by an ~1 day long climactic phase associated with an ~9–12 km high plume (above vent) and a peak MFR of ~10^7 kg s^{-1} (4 and 5 June; Unit I; average MFR of ~7×10^6 kg s^{-1}). For the following 10 days, MFR largely fluctuated but was always $>10^6$ kg s^{-1} (5–14 June; Units II, III, and IV; average MFR of 3×10^6 kg s^{-1}), while the second half of June was characterized by MFR $< 10^6$ kg s^{-1} (15–30 June; average of 2×10^5 kg s^{-1}). Average MFR between 4 and 30 June is 2×10^6 kg s^{-1}. The activity after 30 June was characterized by a several monthlong period of low-intensity plumes. Only the first plume on 4 June could be classified as subplinian, while the rest of the eruption could be defined as small moderate based on MFR, Mdϕ, and LL plots.
2. The height of plumes is clearly controlled by their interaction with the atmosphere and therefore cannot be used as the sole indicator of eruptive conditions at the vent. The scaling parameter Π helps discriminate between strong ($\Pi > 10$), transitional ($0.1 < \Pi < 10$), and weak plumes ($\Pi < 0.1$). Nonetheless, the boundary values of 0.01 and 10 are to be considered as comparative more than absolute, as the calculation of Π strongly depends on the choice of entrainment coefficients.
3. Some of the plumes generated during the 2011 Cordón Caulle eruption, and in particular, those of the climactic phase (i.e., 4 and 5 June), exhibit transitional features between strong and weak plume dynamics with the time scale for wind entrainment term being about 6–8 times faster than the time scale for plume rise in a wind-still environment (i.e., $\Pi = 0.1$–0.2). The periods of 7–12, 14–19, and 23–30 June were associated with weak plumes (i.e., $\Pi = 0.02$–0.1).
4. As shown by satellite images, the sustained plume associated with the first few days of the Cordón Caulle eruption was associated with a series of discrete pulses, which is typical of long-lasting eruptions. Individual pulses could produce puffs with variable height above the ground, which can increase the uncertainty in plume height detection (e.g., 4 June 2011).
5. The VEI and magnitude scale should be used with caution for long-lasting eruptions, and associated values depend on the number of phases considered. Individual layers (i.e., H and K2) range between VEIs 3 and 4, while the cumulative deposit associated with 4–7 June 2011 period of the Cordón Caulle eruption can be classified with VEIs 4 and 5 and a minimum magnitude of 4.8 (including A–F, H, and K2 layers; i.e., total mass/volume of $6.0 \pm 1.1 \times 10^{11}$ kg/1.1 ± 0.2 km^3).
6. Crosswind cloud velocity of 4 June (between 160 and 270 km from vent), 6 June (NE cloud), and 6 June (SE cloud) (between 580 and 950 km from vent) is between 6–10 m s^{-1}, 1–2 m s^{-1}, and 0–1 m s^{-1}, respectively. Downwind cloud velocity of 4 and 6 June (NE cloud) is between 35–45 and 17–21 m s^{-1}, respectively.

7. Cloud spreading associated with transitional plumes, such as those of 4 and 6 June, can be described as a combination of gravitational intrusion, turbulent diffusion, and wind advection. In particular, crosswind spreading for both days can be best described by a linear combination of gravitational spreading and turbulent diffusion with diffusion coefficients in the range of expected values for diffusivity (i.e., 9000 $m^2 s^{-1}$); relative contribution is 49–71% and 40–50% for 4 and 6 June, respectively, with no significant variation with distance from vent. Downwind spreading can be described by a linear combination of gravitational spreading and wind advection, with a relative contribution between 8–19% and 5–9% of total spreading for 2 days, respectively.
8. Our results indicate how the contribution of gravitational spreading can be significant even for small-moderate eruptions characterized by transitional plumes strongly advected by wind and associated with low Richardson number (e.g., 0.003–0.05) and relatively low MFR (e.g., 10^6–10^7 kg s^{-1}); in the case of the first few days of the Cordón Caulle eruption, such a contribution is relevant even in medial to distal regions (100–1000 km from vent).
9. Detailed stratigraphic studies need to be combined with multiple modeling approaches in order to best characterize complex volcanic activity, such as long-lasting eruptions characterized by variable styles and interaction with the surrounding atmosphere.

Acknowledgments

C. Bonadonna was supported by Swiss National Science Foundation (200020_125024). M. Pistolesi and R. Cioni were supported by Italian Ministero Universita' e Ricerca funds (PRIN 2008–AshErupt project). Authors are grateful to A. Bertagnini, R. Gonzales, L. Francalanci, and P. Sruoga for their assistance in the field and to S. Biass for the analysis of ECMWF wind data. The Associate Editor (M. Poland), L. Mastin, and A. Folch are thanked for the thorough and constructive reviews that significantly improved the original manuscript. Data to support this article are available in the supporting information.

References

Alfano, F., C. Bonadonna, A. C. M. Volentik, C. B. Connor, S. F. L. Watt, D. M. Pyle, and L. J. Connor (2011), Tephra stratigraphy and eruptive volume of the May, 2008, Chaitén eruption, Chile, *Bull. Volcanol.*, *73*(5), 613–630, doi:10.1007/s00445-010-0428-x.

Biass, S., and C. Bonadonna (2011), A quantitative uncertainty assessment of eruptive parameters derived from tephra deposits: The example of two large eruptions of Cotopaxi volcano, Ecuador, *Bull. Volcanol.*, *73*(1), 73–90, doi:10.1007/s00445-010-0404-5.

Bonadonna, C., and A. Costa (2012), Estimating the volume of tephra deposits: A new simple strategy, *Geology*, *40*(5), 415–418, doi:10.1130/g32769.1.

Bonadonna, C., and A. Costa (2013a), Plume height, volume, and classification of explosive volcanic eruptions based on the Weibull function, *Bull. Volcanol.*, *75*(8), 1–19, doi:10.1007/s00445-013-0742-1.

Bonadonna, C., and A. Costa (2013b), Modeling of tephra sedimentation from volcanic plumes, in *Modeling Volcanic Processes: The Physics and Mathematics of Volcanism*, edited by S. Fagents, T. Gregg, and R. Lopes, pp. 173–202, Cambridge Univ. Press, Cambridge, U. K.

Bonadonna, C., and J. C. Phillips (2003), Sedimentation from strong volcanic plumes, *J. Geophys. Res.*, *108*(B7), 2340–2368, doi:10.1029/2002JB002034.

Bonadonna, C., J. C. Phillips, and B. F. Houghton (2005a), Modeling tephra sedimentation from a Ruapehu weak plume eruption, *J. Geophys. Res.*, *110*, B08209, doi:10.1029/2004JB003515.

Bonadonna, C., C. B. Connor, B. F. Houghton, L. Connor, M. Byrne, A. Laing, and T. Hincks (2005b), Probabilistic modeling of tephra dispersion: Hazard assessment of a multi-phase eruption at Tarawera, New Zealand, *J. Geophys. Res.*, *110*, B03203, doi:10.1029/2003JB002896.

Bonadonna, C., R. Cioni, M. Pistolesi, C. B. Connor, S. Scollo, L. Pioli, and M. Rosi (2013), Determination of the largest clast sizes of tephra deposits for the characterization of explosive eruptions: A study of the IAVCEI commission on tephra hazard modelling, *Bull. Volcanol.*, *75*(1), 1–15, doi:10.1007/s00445-012-0680-3.

Bonadonna, C., R. Cioni, A. Costa, T. H. Druitt, J. C. Phillips, and L. Pioli (2014), MeMoVolc workshop on the "Dynamics of volcanic explosive eruptions", Consensual Document). [Available at https://vhub.org/resources/3561.]

Bonadonna, C., R. Cioni, M. Pistolesi, M. Elissondo, and V. Baumann (2015), Sedimentation of long-lasting wind-affected volcanic plumes: The example of the 2011 rhyolitic Cordón Caulle eruption, Chile, *Bull. Volcanol.*, *77*(13), 1–19, doi:10.1007/s00445-015-0900-8.

Briggs, G. A. (1972), Chimney plumes in neural and stable surroundings, *Atmos. Environ.*, *6*(7), 507–510, doi:10.1016/0004-6981(72)90120-5.

Bursik, M. (1998), Tephra dispersal, in *The Physics of Explosive Volcanic Eruptions*, edited by J. S. Gilbert and R. S. J. Sparks, pp. 115–144, Geol. Soc., London.

Bursik, M. (2001), Effect of wind on the rise height of volcanic plumes, *Geophys. Res. Lett.*, *28*(18), 3621–3624.

Bursik, M. I., R. S. J. Sparks, J. S. Gilbert, and S. N. Carey (1992), Sedimentation of tephra by volcanic plumes: I. Theory and its comparison with a study of the Fogo A plinian deposit, Sao Miguel (Azores), *Bull. Volcanol.*, *54*, 329–344.

Carazzo, G., E. Kaminski, and S. Tait (2008), On the rise of turbulent plumes: Quantitative effects of variable entrainment for submarine hydrothermal vents, terrestrial and extra terrestrial explosive volcanism, *J. Geophys. Res.*, *113*, B09201, doi:10.1029/2007JB005458.

Carazzo, G., F. Girault, T. Aubry, H. Bouquerel, and E. Kaminski (2014), Laboratory experiments of forced plumes in a density-stratified crossflow and implications for volcanic plumes, *Geophys. Res. Lett.*, *41*, 8759–8766, doi:10.1002/2014GL061887.

Carey, S. N., and R. S. J. Sparks (1986), Quantitative models of the fallout and dispersal of tephra from volcanic eruption columns, *Bull. Volcanol.*, *48*, 109–125.

Castro, J. M., and D. B. Dingwell (2009), Rapid ascent of rhyolitic magma at Chaitén volcano, Chile, *Nature*, *461*(7265), 780–783, doi:10.1038/nature08458.

Castro, J. M., C. I. Schipper, S. P. Mueller, A. S. Militzer, A. Amigo, C. S. Parejas, and D. Jacob (2013), Storage and eruption of near-liquidus rhyolite magma at Cordón Caulle, Chile, *Bull. Volcanol.*, *75*(4), 702–719, doi:10.1007/s00445-013-0702-9.

Collini, E., S. M. Osores, A. Folch, J. G. Viramonte, G. Villarosa, and G. Salmuni (2013), Volcanic ash forecast during the June 2011 Cordón Caulle eruption, *Nat. Hazards*, *66*(2), 389–412, doi:10.1007/s11069-012-0492-y.

Connor, L. G., and C. B. Connor (2006), Inversion is the key to dispersion: Understanding eruption dynamics by inverting tephra fallout, in *Statistics in Volcanology*, edited by H. Mader et al., pp. 231–242, Geol. Soc., London.

Contini, D., A. Donateo, D. Cesari, and A. G. Robins (2011), Comparison of plume rise models against water tank experimental data for neutral and stable crossflows, *J. Wind Eng. Ind. Aerodyn.*, *99*(5), 539–553, doi:10.1016/j.jweia.2011.02.003.

Costa, A., A. Folch, and G. Macedonio (2013), Density-driven transport in the umbrella region of volcanic clouds: Implications for tephra dispersion models, *Geophys. Res. Lett.*, *40*, 4823–4827, doi:10.1002/grl.50942.

Dee, D. P., et al. (2011), The ERA-Interim reanalysis: Configuration and performance of the data assimilation system, *Q. J. R. Meteorol. Soc.*, *137*(656), 553–597, doi:10.1002/qj.828.
Degruyter, W., and C. Bonadonna (2012), Improving on mass flow rate estimates of volcanic eruptions, *Geophys. Res. Lett.*, *39*, L16308, doi:10.1029/2012GL052566.
Degruyter, W., and C. Bonadonna (2013), Impact of wind on the condition for column collapse of volcanic plumes, *Earth Planet. Sci. Lett.*, *377*, 218–226, doi:10.1016/j.eps1.2013.06.041.
Devenish, B. J. (2013), Using simple plume models to refine the source mass flux of volcanic eruptions according to atmospheric conditions, *J. Volcanol. Geotherm. Res.*, *256*, 118–127, doi:10.1016/j.jvolgeores.2013.02.015.
Devenish, B. J., G. G. Rooney, H. N. Webster, and D. J. Thomson (2010), The entrainment rate for buoyant plumes in a crossflow, *Boundary Layer Meteorol.*, *134*(3), 411–439, doi:10.1007/s10546-009-9464-5.
Dufek, J., M. Manga, and M. Staedter (2007), Littoral blasts: Pumice-water heat transfer and the conditions for steam explosions when pyroclastic flows enter the ocean, *J. Geophys. Res.*, *112*, B11201, doi:10.1029/2006JB004910.
Fierstein, J., and W. Hildreth (1992), The plinian eruptions of 1912 at Novarupta, Katmai National Park, Alaska, *Bull. Volcanol.*, *54*, 646–684.
Folch, A., O. Jorba, and J. Viramonte (2008), Volcanic ash forecast: Application to the May 2008 Chaitén eruption, *Nat. Hazards Earth Syst. Sci.*, *8*(4), 927–940.
Fontijn, K., G. G. J. Ernst, C. Bonadonna, M. A. Elburg, E. Mbede, and P. Jacobs (2011), The 4 ka Rungwe Pumice (southwestern Tanzania): A wind-still plinian eruption, *Bull. Volcanol.*, *73*(9), 1353–1368, doi:10.1007/s00445-011-0486-8.
Heffter, J. L. (1965), The variation of horizontal diffusion parameters with time for travel periods of one hour or longer, *J. Appl. Meteorol.*, *4*(1), 153–156.
Hewett, T. A., J. A. Fay, and D. P. Hoult (1971), Laboratory experiments of smokestack plumes in a stable atmosphere, *Atmos. Environ.*, *5*(9), 767–789, doi:10.1016/0004-6981(71)90028-x.
Holasek, R. E., and S. Self (1995), GOES weather satellite observations and measurements of the May 18, 1980, Mount St. Helens eruption, *J. Geophys. Res.*, *100*(B5), 8469–8487, doi:10.1029/94JB03137.
Huq, P., and E. J. Stewart (1996), A laboratory study of buoyant plumes in laminar and turbulent crossflows, *Atmos. Environ.*, *30*(7), 1125–1135, doi:10.1016/1352-2310(95)00335-5.
Inman, D. L. (1952), Measures for describing the size distribution of sediments, *J. Sediment. Petrol.*, *22*, 125–145.
Jay, J., F. Costa, M. Pritchard, L. E. Lara, B. Singer, and J. Herrin (2014), Locating magma reservoirs using InSAR and petrology before and during the 2011–2012 Cordón Caulle silicic eruption, *Earth Planet. Sci. Lett.*, *395*, 254–266.
Mastin, L. G. (2014), Testing the accuracy of a 1-D volcanic plume model in estimating mass eruption rate, *J. Geophys. Res. Atmos.*, *119*, 2474–2495, doi:10.1002/2013JD020604.
Mastin, L. G., et al. (2009), A multidisciplinary effort to assign realistic source parameters to models of volcanic ash-cloud transport and dispersion during eruptions, *J. Volcanol. Geotherm. Res.*, *186*(1–2), 10–21, doi:10.1016/j.jvolgeores.2009.01.008.
Mastin, L. G., A. R. Van Eaton, and J. B. Lowenstern (2014), Modeling ash fall distribution from a Yellowstone supereruption, *Geochem., Geophys., Geosyst.*, *15*(8), 3459–3475, doi:10.1002/2014GC005469.
Morton, B., G. L. Taylor, and J. S. Turner (1956), Turbulent gravitational convection from maintained and instantaneous source, *Proc. R. Soc.*, *234*, 1–23.
Newhall, C. G., and S. Self (1982), The volcanic explosivity index (VEI): An estimate of explosive magnitude for historical volcanism, *J. Geophys. Res.*, *87*(NC2), 1231–1238, doi:10.1029/JC087iC02p01231.
Oddsson, B., M. T. Gudmundsson, G. Larsen, and S. Karlsdottir (2012), Monitoring of the plume from the basaltic phreatomagmatic 2004 Grimsvötn eruption: Application of weather radar and comparison with plume models, *Bull. Volcanol.*, *74*(6), 1395–1407, doi:10.1007/s00445-012-0598-9.
Pasquill, F. (1974), *Atmospheric Diffusion*, 2nd ed., John Wiley, Chichester, U. K.
Pistolesi, M., R. Cioni, C. Bonadonna, M. Elissondo, V. Baumann, A. Bertagnini, L. Chiari, R. Gonzales, M. Rosi, and L. Francalanci (2015), Complex dynamics of small-moderate volcanic events: The example of the 2011 rhyolitic Cordón Caulle eruption, Chile, *Bull. Volcanol.*, *77*(3), 1–24, doi:10.1007/s00445-014-0898-3.
Prejean, S. G., and E. E. Brodsky (2011), Volcanic plume height measured by seismic waves based on a mechanical model, *J. Geophys. Res.*, *116*, B01306, doi:10.1029/2010JB007620.
Pyle, D. M. (1989), The thickness, volume and grain size of tephra fall deposits, *Bull. Volcanol.*, *51*(1), 1–15.
Pyle, D. M. (2000), Sizes of volcanic eruptions, in *Encyclopedia of Volcanoes*, edited by H. Sigurdsson et al., pp. 263–269, Academic Press, San Diego, Calif.
Ripepe, M., C. Bonadonna, A. Folch, D. Delle Donne, G. Lacanna, E. Marchetti, and A. Hoeskuldsson (2013), Ash-plume dynamics and eruption source parameters by infrasound and thermal imagery: The 2010 Eyjafjallajökull eruption, *Earth Planet. Sci. Lett.*, *366*, 112–121, doi:10.1016/j.epsl.2013.02.005.
Scollo, S., S. Tarantola, C. Bonadonna, M. Coltelli, and A. Saltelli (2008), Sensitivity analysis and uncertainty estimation for tephra dispersal models, *J. Geophys. Res.*, *113*, B06202, doi:10.1029/2006JB004864.
Servicio Nacional de Geología y Minería/Observatorio Volcanológico de Los Andes del Sur (2011), Puyehue-Cordón Caulle: Reporte especial de actividad volcánica No. 31, *Rep.* [Available at http://www.sernageomin.cl/volcan.php?pagina=7&ild=38.]
Siebert, L., T. Simkin, and P. Kimberly (2010), *Volcanoes of the World*, Univ. of Calif. Press, Berkeley.
Sparks, R. S. J., M. I. Bursik, S. N. Carey, J. S. Gilbert, L. S. Glaze, H. Sigurdsson, and A. W. Woods (1997), *Volcanic Plumes*, 574 pp., John Wiley, Chichester, U. K.
Suzuki, Y. J., and T. Koyaguchi (2010), Numerical determination of the efficiency of entrainment in volcanic eruption columns, *Geophys. Res. Lett.*, *37*, L05302, doi:10.1029/2009GL042159.
Suzuki, Y. J., and T. Koyaguchi (2013), 3-D numerical simulation of volcanic eruption clouds during the 2011 Shinmoedake eruptions, *Earth Planets Space*, *65*(6), 581–589, doi:10.5047/eps.2013.03.009.
Tuffen, H., M. R. James, J. M. Castro, and C. I. Schipper (2013), Exceptional mobility of an advancing rhyolitic obsidian flow at Cordón Caulle volcano in Chile, *Nat. Commun.*, *4*, 2709, doi:10.1038/ncomms3709.
Tupper, A., and R. Wunderman (2009), Reducing discrepancies in ground and satellite-observed eruption heights, *J. Volcanol. Geotherm. Res.*, *186*(1–2), 22–31, doi:10.1016/j.jvolgeores.2009.02.015.
Valentine, G. A., and K. H. Wohletz (1989), Numerical models of plinian eruption columns and pyroclastic flows, *J. Geophys. Res.*, *94*(B2), 1867–1887, doi:10.1029/JB094iB02p01867.
Volentik, A. C. M., C. Bonadonna, C. B. Connor, L. J. Connor, and M. Rosi (2010), Modeling tephra dispersal in absence of wind: Insights from the climactic phase of the 2450 B.P. plinian eruption of Pululagua volcano (Ecuador), *J. Volcanol. Geotherm. Res.*, *193*(1–2), 117–136, doi:10.1016/j.jvolgeores.2010.03.011.

Walker, G. P. L., and R. Croasdale (1971), Two plinian-type eruptions in the Azores, *J. Geol. Soc. London*, *127*, 17–55.
Whittington, A. G., A. M. Hofmeister, and P. I. Nabelek (2009), Temperature-dependent thermal diffusivity of the Earth's crust and implications for magmatism, *Nature*, *458*(7236), 319–321, doi:10.1038/nature07818.
Wicks, C., J. C. de la Llera, L. E. Lara, and J. Lowenstern (2011), The role of dyking and fault control in the rapid onset of eruption at Chaitén volcano, Chile, *Nature*, *478*(7369), 374−377, doi:10.1038/nature10541.
Woodhouse, M. J., A. J. Hogg, J. C. Phillips, and R. S. J. Sparks (2013), Interaction between volcanic plumes and wind during the 2010 Eyjafjallajökull eruption, Iceland, *J. Geophys. Res. Solid Earth*, *118*, 92–109, doi:10.1029/2012JB009592.
Woods, A. W. (1988), The fluid dynamics and thermodynamics of eruption columns, *Bull. Volcanol.*, *50*(3), 169–193.